LRRC23 truncation impairs radial spoke 3 head assembly and sperm motility underlying male infertility

Jae Yeon Hwang[1,10,†], Pengxin Chai[2,†], Shoaib Nawaz[3,11,†], Jungmin Choi[4,5], Francesc Lopez-Giraldez[6], Shabir Hussain[7,12], Kaya Bilguvar[4,6], Shrikant Mane[6], Richard P. Lifton[8], Wasim Ahmad[3,7], Kai Zhang[2], Jean-Ju Chung[1,9,*]

[1]Department of Cellular and Molecular Physiology, Yale School of Medicine, Yale University, New Haven, CT, 06510; [2]Department of Molecular Biophysics and Biochemistry, Yale School of Medicine, Yale University, New Haven, CT, 06510; [3]Department of Biotechnology, Faculty of Biological Sciences, Quaid-i-Azam University, 45320, Islamabad, Pakistan; [4]Department of Genetics, Yale School of Medicine, Yale University, New Haven, CT, 06510; [5]Department of Biomedical Sciences, Korea University College of Medicine, Seoul, South Korea, 02841; [6]Yale Center for Genome Analysis, Yale University, West Haven, CT, 06516; [7]Department of Biochemistry, Faculty of Biological Sciences, Quaid-i-Azam University, 45320, Islamabad, Pakistan; [8]Laboratory of Human Genetics and Genomics, The Rockefeller University, New York, NY, 10065; [9]Department of Obstetrics, Gynecology and Reproductive Sciences, Yale School of Medicine, Yale University, New Haven, CT, 06510; [10]Present address, Department of Molecular Biology, Pusan National University, Pusan, South Korea, 43241; [11]Present address, Department of Human Genetics, Sidra Medicine, Doha, Qatar, 26999; [12]Present address, Clinical and Molecular Metabolism Program, Faculty of Medicine, University of Helsinki, Helsinki, Finland, 00250

[†]These authors contributed equally to this work.

*Correspondence to Jean-Ju Chung: jean-ju.chung@yale.edu

Keywords: Male infertility, WES, Sperm flagella, Radial spoke, Cryo-ET

Abstract

Radial spokes (RS) are T-shaped multiprotein complexes on the axonemal microtubules. Repeated RS1, RS2, and RS3 couple the central pair to modulate ciliary and flagellar motility. Despite the cell type specificity of RS3 substructures, their molecular components remain largely unknown. Here, we report that a leucine-rich repeat-containing protein, LRRC23, is an RS3 head component essential for its head assembly and flagellar motility in mammalian spermatozoa. From infertile male patients with defective sperm motility, we identified a splice site variant of *LRRC23*. A mutant mouse model mimicking this variant produces a truncated LRRC23 at the C-terminus that fails to localize to the sperm tail, causing male infertility due to defective sperm motility. LRRC23 was previously proposed to be an ortholog of the RS stalk protein RSP15. However, we found that purified recombinant LRRC23 interacts with an RS head protein RSPH9, which is abolished by the C-terminal truncation. Our comparative sequence analyses also showed that LRRC34, not LRRC23, is the RSP15 ortholog. Cryo-electron tomography clearly revealed that the absence of the RS3 head and the sperm-specific RS2-RS3 bridge structure in LRRC23 mutant spermatozoa. Our study provides new insights into the structure and function of RS3 in mammalian spermatozoa and the molecular pathogenicity of LRRC23 underlying reduced sperm motility in infertile human males.

Introduction

Motile cilia and flagella are evolutionarily conserved organelles essential for cellular motility (Inaba, 2011; Ishikawa, 2017). The core of motile cilia and flagella is the '9+2' axoneme, characterized by a scaffold structure composed of nine peripheral microtubule doublets (MTDs) and a central pair of singlet microtubules (CP). Each MTD binds two rows of dyneins, the outer-arm dyneins (OAD) and inner-arm dyneins (IAD), which generate mechanical force required for the ciliary beating via ATP hydrolysis (Kubo et al, 2021; Rao et al, 2021). Radial spoke (RS) controls the amplitude of the ciliary and flagellar beat by transmitting mechanochemical signals from the CP to the axonemal dyneins (Smith & Yang, 2004; Viswanadha et al, 2017). In *Chlamydomonas reinhardtii*, RS mutations paralyze the flagellar movement (Witman et al, 1978) and the axoneme lacking RS system shows reduced velocity of microtubule sliding by dyneins (Smith & Sale, 1992). In human and mouse, mutations in RS components or their absence cause primary ciliary dyskinesia (PCD) and/or male infertility due to the defective ciliary and flagellar beating (Abbasi et al, 2018; Liu et al, 2021; Sironen et al, 2020). These studies highlight the physiological importance of RS in regulating ciliary and flagellar movement.

A triplet of three RSs (RS1, RS2, and RS3) repeats every 96-nm along the peripheral MTDs and this 96-nm periodicity of RS is well-conserved in cilia and flagella across diverse organisms (Viswanadha et al, 2017; Zhu et al, 2017). RS is a multiprotein complex; at least 23 RS components were identified in *C. reinhardtii* (Gui et al, 2021; Viswanadha et al, 2017; Yang et al, 2006). These RS components are also crucial for RS organization and function in other ciliated and flagellated organisms (Bazan et al, 2021; Ralston et al, 2006; Sironen et al, 2020; Urbanska et al, 2015), indicating evolutionarily conserved molecular composition of the RS. However, cryo-electron microscopy (cryo-EM) studies have revealed species- and tissue-specific structural variabilities in RS3. For example, RS3 in most species is a T-shaped axonemal structure that consists of a head and a stalk like those of RS1 and RS2 (Imhof et al, 2019; Leung et al, 2021; Lin et al, 2014; Pigino et al, 2011) but RS3 in *C. reinhardtii* is a headless and stump-like structure (Pigino et al, 2011). In addition, mammalian sperm flagellar axoneme carries a unique bridge structure between RS2 and RS3 (Leung et al, 2021), which is not observed from tracheal cilia as well as other flagellated organisms (Imhof et al, 2019; Lin et al, 2014). This variability suggests that RS3 is an evolutionarily more divergent structure and conveys species- and/or tissue-specific ciliary and flagellar function. Yet, the overall molecular composition of RS3 and the extent to which RS3 components are species- and/or tissue specific remains largely unknown.

Asthenozoospermia (ASZ) is the male infertility classified by reduced sperm motility (World Health Organization, 2010). ~80% of male infertile patients manifest sperm motility defects (Curi et al, 2003) as infertile male with abnormal sperm morphology and/or reduced sperm count often accompany low motility (Cavarocchi et al, 2022; Toure et al, 2021). Recent whole exome sequencing studies identified genetic defects in RS components from idiopathic ASZ patients (Liu et al, 2021; Martinez et al, 2020; Shen et al, 2021). Mutant analyses using model organisms further elucidated the function of RS components in the flagellar movement and the pathogenic mechanisms (Liu et al, 2021; Martinez et al, 2020). Thus, WES combined with functional and structural analyses of mutants, especially in a mouse model, would be a powerful and direct approach to understand mammalian specific RS3 roles including sperm motility regulation and genetic etiologies causing male infertility.

Here, we report a bi-allelic loss-of-function splicing variant in *LRRC23* from ASZ patients in a Pakistani consanguineous family. We generated a mouse model that mimics the human mutation and found that the mutation leads to C-terminal truncated LRRC23 and that the mutant mice

phenocopy the impaired sperm motility and male infertility. Using biochemical analyses and structural prediction, we showed that, different from previously known, LRRC23 is not the ortholog of a RS2 stalk protein RSP15 but interacts with a known RS head protein. Finally, we visualized the in-cell structures of RS triplets in intact WT and mutant sperm using cryo-electron tomography (cryo-ET). We observed missing RS3 head and aberrant junction between RS2 and RS3 in the mutant flagellar axoneme, unarguably demonstrating that LRRC23 is a head component of RS3. This study provides molecular pathogenicity of *LRRC23* in RS-associated ASZ and reveals unprecedented structural insights into the RS3 and its implication in normal sperm motility and male fertility in mammals.

Results

A Loss of Function Splice Site Variant Truncating LRRC23 is Identified from a Consanguineous Family with Asthenozoospermia

A consanguineous Pakistani family with infertile males was recruited (Fig 1 A). Both infertile males (IV-1 and IV-2) have failed to have child over 3 years of unprotected sex after marriage (Table S1). The male infertile patients do not show PCD-related symptoms, abnormal heights, weights, secondary characteristics, nor anatomical defects. They also have normal karyotypes without Y chromosome microdeletion. Overall, Papanicolaou (PAP)-stained spermatozoa from the infertile patients showed only subtle morphological defects (Figs 1B and EV1A), which was further supported by clinical semen analyses (Table EV1). However, their progressive motility was lower than the World Health Organization (WHO) standard (World Health Organization, 2010) and the patients were clinically diagnosed as ASZ (Table EV1). To understand the genetic etiology underlying the defective sperm motility, we performed whole exome sequencing (WES) on the proband, IV-1. WES estimated 5.02% inbreeding co-efficiency and the longest homozygous-by-descent segment as 37.5 cM, verifying the consanguineous nature of the recruited family. Among the four identified rare variants (Table EV2), only one homozygous splicing donor site variant (c.621+1G>A) in *LRRC23* (leucin-rich repeat containing protein 23) is co-segregated with the male infertility phenotype (Fig 1A, C, and D). Of note, a female sibling (IV-4) who also has the homozygous *LRRC23* variant (IV-4) is infertile because her partner was able to have children from his second marriage (Fig 1A). However, the infertility of IV-4 would not be due to the variant because the mother (III-1) also carries the homozygous allele but was fertile (Fig 1A). The variant at the splicing donor site of *LRRC23* intron 5 is predicted to prevent splicing out of the intron, which can lead to early termination of protein translation with loss of 136 amino acids at the C-terminus (Fig EV1B and C). To verify the splicing defects and generation of mutant protein by the variant, we constructed minigenes to express *LRRC23* ORF spanning partial intron 5 with the normal or variant sequence at the splicing site in 293T cells (Fig 1E). 293T cells transfected with the construct carrying the variant failed to splice out the intronic region (Fig 1F) and generated only truncated LRRC23 (Fig EV1D). These results suggest the variant is pathogenic and explains the male infertility with defective sperm motility in this family.

C-terminally Truncated LRRC23 Fails to Localize in the Flagella and Causes Defective Sperm Motility

LRRC23 is a radial spoke (RS) component (Padma et al, 2003). Consistent with the ASZ phenotype in our infertile patients with a new splice mutation in *LRRC23*, genetic ablation of *Lrrc23* in mice causes severe sperm motility defects and male infertility (Zhang et al, 2021). However, how the C-terminus truncation of LRRC23 affects the RS structure and function remains unresolved. To better understand detailed function of LRRC23 and the molecular pathogenicity of the identified variant, we generated *Lrrc23* mutant mice by CRISPR/Cas9 genome editing to mimic the predicted outcome in human patients (Figs EV1 and EV2A). We targeted two regions, one in intron 5 and the other in intron 7 (Fig EV2B) to delete exon 6 and 7 together and express truncated LRRC23 at C-terminus. We established two mouse lines with 4,126 or 4,135 bp deletion (*Lrrc23-4126del* and *Lrrc23-4135del*, respectively) (Fig EV2C). Both homozygous *Lrrc23-4126del* and *4135del* mice displayed the identical male infertility and defective sperm motility phenotypes in our initial characterization. In this study, we used *Lrrc23-4126del* line as *Lrrc23-mutant* line unless indicated. We observed that truncated *Lrrc23* mRNA is expressed from the mutant *Lrrc23* allele but the total mRNA level of *Lrrc23* in testis is not different from wildtype (WT) to that in *Lrrc23*$^{\Delta/\Delta}$ males (Fig EV2D-F). Sequencing the truncated *Lrrc23* mRNA revealed that the transcript would produce mutant LRRC23 containing 27 non-native amino acids translated from 3' UTR instead of 136 amino acids at the C-terminus (Fig EV2G). Despite the comparable *Lrrc23* mRNA levels in WT and

Lrrc23$^{\Delta/\Delta}$ testis, the truncated LRRC23 is detected only marginally in the microsome fraction of *Lrrc23*$^{\Delta/\Delta}$ testis, different from full-length LRRC23 enriched in the cytosolic fraction of WT testis (Figs 2A and EV3A and B). In addition, the mutant LRRC23 is not present in epididymal sperm (Figs 2B and C, and EV3C-E)**,** indicating that the C-terminal region is essential for proper LRRC23 transportation to the sperm flagella.

Sperm from *Lrrc23*$^{\Delta/\Delta}$ and *Lrrc23-4135del*$^{\Delta/\Delta}$ males are morphologically normal (Figs 2C and EV3E and F) and the epididymal sperm counts of *Lrrc23*$^{+/\Delta}$ and *Lrrc23*$^{\Delta/\Delta}$ males are not significantly different (Fig 2D). Despite the normal morphology and sperm counts, *Lrrc23*$^{\Delta/\Delta}$ males are 100% infertile (Fig 2E and F). To further understand how the homozygous *Lrrc23* mutation causes male infertility, we performed Computer Assisted Semen Analysis (CASA). *Lrrc23*$^{\Delta/\Delta}$ sperm motility parameters are significantly altered compared to *Lrrc23*$^{+/\Delta}$ sperm (Fig EV3G). *Lrrc23*$^{\Delta/\Delta}$ sperm cannot swim efficiently under viscous conditions that mimic the environment in female reproductive tract (Fig 2G; Movie EV1), and their flagella just vibrate but do not beat normally (Figs 2H and EV3H; Movie EV2). In addition, inducing capacitation did not rescue any observed motility defect of *Lrrc23*$^{\Delta/\Delta}$ sperm as demonstrated by flagellar waveform analysis, and CASA measurement of curvilinear velocity (VCL), straight line velocity (VSL), and amplitude of lateral head (ALH). These results suggest the C-terminal truncation dysregulates the flagellar localization of the mutant LRRC23, leading to sperm motility defects and male infertility.

C-terminal Truncation of LRRC23 Abolishes its Interaction with Radial Spoke Head

Recent cryo-ET studies revealed that T-shaped RS structures (i.e., head and stalk) are conserved across the species (Leung et al, 2021; Lin et al, 2014) (Fig. 3 A). Three RSs (RS1, RS2, and RS3) are repeated in a 96-nm interval along the flagellar axoneme in mammalian sperm, sea urchin sperm, *Trypanosoma brucei*, and even in *C. reinhardtii* with stump-like RS3 without a head structure (Fig. 3 A). LRRC23 is a RS protein in chordate axoneme and has been considered especially as the orthologue of RSP15, a RS2 stalk protein in *C. reinhardtii* (Han et al, 2018; Satouh & Inaba, 2009; Yang et al, 2006; Zhang et al, 2021) (Fig 3B). We initially hypothesized the C-terminal truncation of LRRC23 affects the assembly of a RS stalk and/or its incorporation into the RS2. Thus, we tested the protein-protein interaction of normal (hLRRC23^{WT}) and mutant (hLRRC23^{Mut}) human LRRC23 with known RS stalk (RSPH3, RSPH22) or head (RSHP6A, RSHP9) proteins using RSPH-trap assay (Figs 3C-E and EV4A). Purified GST-tagged hLRRC23^{WT} and hLRRC23^{Mut} proteins (Fig 3C and D) were incubated with a recombinant human RSPH enriched by immunoprecipitation (Fig 3E). This trap assay demonstrated that hLRRC23^{WT} interacts only with RSPH9, a RS head protein, among the head and stalk RSPH proteins tested (Figs 3F and EV4B). Markedly, hLRRC23^{Mut} does not interact with RSPH9, indicating LRRC23 interaction with RS head via its C-terminus. This result also raises the question whether LRRC23 is a head protein of RS, not a stalk protein, a different picture from previous studies. To test this new hypothesis, we performed BLAST search and found *C. reinhardtii* RSP15 (Gui et al, 2021) has the highest sequence homology to LRRC34, not LRRC23, in *Ciona intestinalis*. Our phylogenetic and pairwise distance comparison analyses also revealed that LRRC34 orthologs are evolutionarily closer to RSP15 orthologs than LRRC23 orthologs (Figs 3G and EV4C). Moreover, AlphaFold-predicted structure of human LRRC34, but not that of LRRC23, presents the same structural features as those of RSP15 (i.e., repeated leucin-rich repeat domains and an α-helix motif in-between) (Fig 3H). *LRRC34* and *LRRC23* share their gene expression patterns among tissues, most abundantly expressed in the tissues known for ciliary and flagellar function such as retina, testis, and fallopian tube (Fig EV4D and E). All these results suggest that LRRC34 is a ciliary and flagellar protein and likely the RSP15 orthologue in chordates, and that LRRC23 function is associated with the RS head.

LRRC23 Mutation Disorganizes Radial Spoke 3 in Sperm Flagella

Next, we examined the impact of LRRC23 loss of function by the C-terminal truncation on the subcellular and ultrastructural organization of sperm. We first compared flagellar compartmentalization between *Lrrc23*$^{+/\Delta}$ and *Lrrc23*$^{\Delta/\Delta}$ sperm. Confocal imaging of immunostained sperm by antibodies against various proteins of known localization did not show any difference on the subflagellar localization of axonemal or peri-axonemal proteins (Fig 4A and EV5A). The levels of such flagellar proteins are also not significantly different between *Lrrc23*$^{+/\Delta}$ and in *Lrrc23*$^{\Delta/\Delta}$ sperm (Fig EV5B and C). Furthermore, transmission electron microscopy (TEM) did not reveal apparent structural abnormalities in *Lrrc23*$^{\Delta/\Delta}$ sperm flagella (Figs 4B and EV5D). These results indicate overall subflagellar and ultrastructural organization in *Lrrc23*$^{\Delta/\Delta}$ sperm is preserved despite almost complete loss of sperm motility. Any structural abnormality in *Lrrc23*$^{\Delta/\Delta}$ sperm would be subtle and local in the axoneme, likely in the RS head region, which requires a higher resolution microscope technique.

To determine how the absence of LRRC23 affects sperm structure in more detail, we performed cryo-ET 3D reconstruction to visualize substructural changes of the sperm axoneme (Fig 4C and Movie EV3). The reconstructed tomogram slices revealed striking details of the RS structural difference between WT sperm and *Lrrc23*$^{\Delta/\Delta}$ sperm (Fig 4C). In WT sperm, the three RSs are repeated with a typical pattern, in which RS1 and RS2 are recognized by an additional EM density between them (barrel structure, Leung et al, 2021) followed by RS3 (Fig 4C, *left*). In *Lrrc23*$^{\Delta/\Delta}$ sperm, EM densities corresponding to RS3 are significantly weaker than those in WT sperm whereas the structural features of RS1 and RS2 are overall kept unaltered from that of WT sperm (Fig 4C*, right*). These results strongly indicate that the LRRC23 mutation specifically disorganizes RS3 in the sperm axoneme.

LRRC23 Is a Head Component of Radial Spoke 3

To visualize the structural defects of RS3 along the *Lrrc23*$^{\Delta/\Delta}$ sperm axoneme in more detail (Fig 4C), we performed sub-tomogram averaging (STA) of the axonemal doublets in 96 nm repeat (i.e., the distance that spans a single set of RS1, RS2, and RS3) on both WT and *Lrrc23*$^{\Delta/\Delta}$ spermatozoa (Figs 5 and EV6). Remarkably, the resulting 3D maps reveal that the head region of RS3 is entirely missing in *Lrrc23*$^{\Delta/\Delta}$ sperm whereas the heads of RS1 and RS2 are intact (Fig 5A and B). In addition, superimposition of the 3D STA maps demonstrates that the junctional structure between RS2 and RS3–present in mouse and human sperm but not in *C. reinhardtii* nor in *T. brucei* flagellar axoneme–is also specifically abolished in *Lrrc23*$^{\Delta/\Delta}$ sperm (Fig 5C). By contrast, *Lrrc23*$^{\Delta/\Delta}$ sperm have intact stalk structures of RS3 like those in WT sperm. Consistent with the protein-protein interaction between LRRC23 and the RS head protein RSPH9 using the RSPH-trap approach (Fig 3), these direct structural observations unarguably clarify that LRRC23 is a RS3 head component and the absence of the RS3 head leads to motility defects in *Lrrc23*$^{\Delta/\Delta}$ sperm. These results demonstrate that the C-terminal truncation of LRRC23 prevents the assembly of RS3 head during spermatogenesis, thus preventing functional RS3 complex formation. Taken together, our functional and structural studies using the mouse model recapitulating the human mutation elucidate the molecular pathogenicity of LRRC23 underlying impaired sperm motility and male infertility (Fig 5D).

Discussion

LRRC23 is a Distinct Head Component of Radial Spoke 3

Accumulating evidence on the structural heterogeneity of radial spokes in cilia and flagella suggests that the molecular organization and function of RS3 is distinct from those of RS1 and RS2. For example, the morphology of RS3 head is distinguished from those of RS1 and 2 in mouse motile cilia (Zheng et al, 2021). Moreover, in the tracheal cilia of the PCD patients, RSPH1 or RSPH4 loss-of-function mutation specifically abolished RS1 and RS2 heads, but not RS3 head (Lin et al, 2014; Zhao et al, 2021) even though RS3 shares T-shaped structure just like RS1 and RS2 in most eukaryotic motile cilia and flagella (Imhof et al, 2019; Leung et al, 2021; Lin et al, 2012; Lin et al, 2014). Despite these findings, the molecular composition of RS3 head remains largely unknown. The current study demonstrates that LRRC23 is a RS3-specific head component. Previous immuno-EM studies showed that LRRC23 is a conserved RS protein in *C. intestinalis* and mouse (Pigino et al, 2011; Zhang et al, 2021). It is of note that LRRC23 was originally predicted to be the orthologue of RSP15 in *C. reinharditti*, a RS2 stalk protein, due to the presence of leucine-rich repeat domains (Gui et al, 2021; Yang et al, 2006). Yet, we found LRRC23 orthologues are not conserved in *C. reinharditti* in which RS3 is headless and short stump-like, but present in the species where RS3 head structure is preserved, such as *T. thermophila*, sea urchin, and mammals. Instead of LRRC23, our phylogenetic and structural comparison strongly suggests that LRRC34 is likely the RSP15 orthologue in chordate animals (Figs 3 and EV4) and a previously unappreciated component of RS2 stalk. Identifying a LRRC34 loss-of-function mutation from ciliopathic children further supports that LRRC34 is a RSP component (Shamseldin et al, 2020). Our wild type-mutant comparison approach using cryo-ET analyses ultimately clarify that LRRC23 is required for assembling the RS3 head structure (Figs 4 and 5), indicating LRRC23 as a RS3 head component. Interestingly, a RS head component, RSPH9, interacts with LRRC23 but the protein level or the localization of RSPH9 is not altered in *Lrrc23*$^{\Delta/\Delta}$ sperm (Fig EV4), suggesting that RSPH9 is a head component of RS1 and RS2 like in *C. reinhardtii* (Gui et al, 2021), but not of RS3. Of note is that an independent study reported that LRRC23 is required for flagellar localization of the RS stalk and fibrous sheath components in mature sperm (Zhang et al, 2021). This discrepancy between two studies is likely due to the presence of the truncated LRRC23 in testis in *Lrrc23*$^{\Delta/\Delta}$ males, which might partly allow flagellar localization of other flagellar components during germ cell development. Although the full picture of molecular composition of RS3 head remains to be revealed, our findings demonstrate LRRC23 is a RS3-specific head component. This conclusion is further supported by the presence of LRRC23 in tracheal cilia (Zhang et al, 2021) that lack the RS2-RS3 bridge structure (Leung et al, 2021).

LRRC23 is required for mammalian sperm-specific bridge structure between RS2 and RS3

In motile cilia and flagella, a set of three RSs is repeated along the axoneme (Leung et al, 2021; Lin et al, 2012; Lin et al, 2014; Viswanadha et al, 2017). Notably, a recent cryo-ET study revealed additional RS substructures in mammalian sperm flagella, a barrel structure at RS1 and a junctional bridge structure between RS2 and RS3 (Leung et al, 2021), which were not observed in the sea urchin sperm or human motile cilia (Lin et al, 2014). Furthermore, they are asymmetrically distributed along the mammalian sperm axoneme, corresponding to the peripheral MTDs in a species-specific manner (Chen et al, 2023). Our cryo-ET and STA analyses visualized the mammalian sperm-specific RS1 barrel and RS2-RS3 bridge structures in WT sperm flagella, consistent with Leung et al (Leung et al, 2021). Strikingly, in *Lrrc23* mutant sperm, most of the EM density corresponding to the RS2-RS3 bridge structure is missing and/or altered together with that of the RS3 head (Figs 4 and 5). Considering the absence of RS2-RS3 bridge in tracheal cilia (Lin et al, 2014), LRRC23 also contributes to assemble this flagellar RS substructure. Thus, we speculate that the RS3 and RS2-RS3 bridge structures and their sub-axonemal localization confer non-planar and asymmetric flagellar motility unique to mammalian sperm hyperactivation. As the RS2-RS3 bridge structure is absent in tracheal cilia (Lin et al, 2014), our study unambiguously demonstrates that LRRC23 is required for assembling this bridge structure specifically in mammalian sperm flagella. If so, LRRC23 may be localized at the junction between RS2-RS3

bridge structure and RS3 head. The detailed molecular components that comprise the RS2-RS3 bridge requires further study. Profiling and comparing LRRC23 interactomes from mammalian motile cilia and sperm flagella could unveil the cell-type specific molecular organization of RS3.

LRRC23 loss of function causes male infertility in mice and human

Loss-of-function mutations in various RS components that are common to motile cilia and sperm flagella were reported to cause PCD and/or male infertility. Loss-of-function mutations of RSPH1 (Knowles et al, 2014; Kott et al, 2013), RSPH3 (Jeanson et al, 2015), RSPH4A and RSPH9 (Castleman et al, 2009) were identified from PCD patients. Some of the male patients carrying RSPH1 and RSPH3 mutations were infertile (Jeanson et al, 2015; Knowles et al, 2014). RSPH1, RSPH4A, and RSPH9 knockout mouse models recapitulated the PCD phenotypes such as hydrocephalus and impaired mucociliary clearance (Yin et al, 2019; Yoke et al, 2020; Zou et al, 2020). However, there are other RS components in which mutations only cause male infertility in mice and human. For example, WES of infertile males without PCD symptoms identified mutations in CFAP251 (Auguste et al, 2018; Kherraf et al, 2018) and CFAP61 (Liu et al, 2021; Ma et al, 2021). RSPH6 (Abbasi et al, 2018), CFAP251 (Kherraf et al, 2018), or CFAP61 (Liu et al, 2021) deficiency also rendered male mice infertile but without gross abnormalities. These phenotypic differences could be due to a different physiological role of the individual RS component between motile cilia and flagella or a distinct repertoire of the RS components that permits functional redundancy. In our study, LRRC23 mutant mice do not have any apparent gross abnormality but display male infertility (Fig 2). This observation is in line with the previous report by Zhang et al in which the authors noted normal tracheal ciliary beat but immotile sperm in the absence of LRRC23 (Zhang et al, 2021). Supportive of these observations, the infertile male patients in the current study do not show PCD symptoms. This phenotype of male infertility without PCD symptoms in both mice and human suggests the mammalian sperm-specific role of LRRC23 in RS structure and function. Physiological implication of LRRC23 and RS3 in motile cilia is unclear but it is likely dispensable for normal ciliary movement probably due to compensatory and/or redundant RS3 proteins specific to cilia. Whether LRRC23 absence would lead to similar structural aberration in RS3 head of motile cilia requires further study. Intriguingly, LRRC23 loss-of-function impairs primarily flagellar motility but morphology only marginally, which is in distinct from other RS components. For example, the absence of RSPH6, CFAP251, or CFAP61 causes male infertility without PCD symptoms but displays multiple morphological abnormalities of the flagella characterized by absent, short, bent, coiled, and irregular flagella (Toure et al, 2021). By contrast, LRRC23 mutation and absence do not cause either PCD nor MMAF phenotypes in human and mouse, suggesting a distinct physiological significance of LRRC23 in reduced sperm motility.

Materials and Methods

Subject and family

This study was approved from the review board of Quaid-i-Azam University, Islamabad, Pakistan (IRB00003532, IRB protocol # QAU-171) and the Yale Center for Mendelian Genomics. The family members recruited in this study were explained about the procedure and possible outcomes. The family members provided written consent to attend this study.

Sample collection and clinical investigation

Semen Semen samples were collected and clinically analyzed according to WHO guidelines (World Health Organization, 2010). Semen samples were collected from the infertile male members after 2-5 days of abstinence from sexual intercourse. The collected semen samples were subjected to the clinical analysis by expert laboratory technologists at Aga Khan Medical Centre (Gilgit, Pakistan) to measure pH, volume, viscosity, and color of the semen and sperm parameters. To assess sperm motility and morphology, the collected semen was liquefied at 37 °C for 30-60 minutes. A minimum of 1,000 spermatozoa were counted to analyze sperm motility by the CASA system using an MTG-GmbH analyzer (version 5.4; MTG-MedeaLAB) according to the unit's standard operating procedures based on the WHO guidelines as previously reported (Krause et al, 2016; Nawaz et al, 2021; Slabbert et al, 2015). Sperm from liquified semen were subjected to PAP-staining and the morphology was microscopically analyzed according to the guidelines from WHO and evaluated by a reproductive medicine specialist. PAP-stained sperm were imaged using CMOS camera (Basler acA1300-200μm, Basler AG) equipped in Nikon E200 microscope.

Blood Venous blood samples were collected from attending family members. Collected blood samples were used for karyotyping and genomic DNA extraction. Blood cells cultured with phytohemagglutinin for 72 hours were used for karyotyping. The cultured cells were disrupted and Giemsa-stained. Twenty metaphases were examined to examine karyotypes of each member. Genomic DNA (gDNA) samples were extracted using QIAamp DNA Kit (QIAGEN, Germany). Extracted gDNA samples were subjected to examine microdeletions at the Y-chromosome (AZFa, AZFb, AZFc, and AZFd), whole exome sequencing (WES), and Sanger Sequencing.

Whole-Exome Sequencing and Data Analysis

Whole exome sequencing was carried out as described in our previous study (Hwang et al, 2021b). Briefly, 1.0 µg of genomic DNA from proband's blood is fragmented to an average length of 140 bp using focused acoustic energy (Covaris E210). DNA fragments were subjected to exome capturing using the IDF xGen capture probe panel with an additional "spike-in" of ~2,500 region which are total 620 kb of RefGene coding regions. The captured fragments were pair-end sequenced by 101 bp reading using NovaSeq 6000 with S4 flow cell (Illumina). Sequenced reads were aligned to reference human genome (GRCh37/hg19) using the BWA-MEM (Li, 2013) and processed to generate variants using GATK v3.4 (McKenna et al, 2010; Van der Auwera et al, 2013). Variants were annotated with ANNOVAR (Wang et al., 2010) and the predicted deleteriousness of non-synonymous variants was determined by MetaSVM (Dong et al, 2015). Either loss of function mutations of stop-gains, stop-losses, frameshift indels, and canonical splice-sites or deleterious missense mutations predicted by MetaSVM were considered to potentially damaging. Recessive variants of which MAF values in Genome Aggregation Database (gnomeAD), v2.1 (Lek et al, 2016; https://gnomad.broadinstitute.org/) are lower than 10^{-3} were considered for rare variants. Rare damaging variants were further filtered to exclude false-positives using the follow criteria: (1) PASS for GATK variant quality score recalibration, (2) MAF ≤ 2.0 x 10^{-5} in the gnomAD, (3) DP ≥ 8

396 independent reads, (4) GC score ≥ 20, (5) MQ score ≥ 40, (6) PLdiff/DP ≥ 8, and (7) indels in Low
397 Complexity Regions. Co-segregation of candidate variants with the phenotypes were confirmed by
398 genomic DNA PCR and Sanger sequencing. Genomic DNA PCR was performed with using
399 One*Taq*® 2X Master Mix (NEB) and used primer pairs were; Fwd: 5'-
400 GCTGAGCATTTGGAGTGGC-3' and Rev: 5'-CCTGCTAGGTGGCTGTGTAT-3' for *LRRC23*, Fwd:
401 5'-TGAACCCCTGGCACAACT-3' and Rev: 5'-TTTTTACTCAGCGATACCACATTCACAG-3' for
402 *SCN5A*, Fwd: 5'- TGGCTAAATCCCATCCAGTCC-3' and Rev: 5'- GAGTCTGTCCTTGCCCGTAG-
403 3' for *NOX1,* and Fwd: 5'-GATTGTCATCGCCTTGTTCATC-3' and Rev: 5'-
404 TGTTTTGTGGTGGCACAGTC-3' for *PRRG3*. Amplified PCR products were subjected to Sanger
405 sequencing.
406
407 **Kinship Analysis**
408 Kinship coefficient was estimated to confirm pedigree information and pairwise relatedness of
409 proband using KING v2.2.4 (Manichaikul et al, 2010). Inbreeding coefficient was calculated by
410 homozygosity-by-descent (HBD). HBD segment in the proband was detected by Beagle v3.3.2
411 (Browning & Browning, 2011). Homozygosity in segments over 2 cM was considered for
412 consanguinity.
413
414 **Animals**
415 Wildtype C57BL/6 mice were from Charles River Laboratory. Mice were cared in accordance with
416 the guidelines approved by Institutional Animal Care and Use Committee (IACUC) for Yale
417 University (#20079).
418
419 **Generation of the *Lrrc23*-mutant mice and genotyping**
420 *Lrrc23*-mutant mice were generated on C57BL/6 background using CRISPR/Cas9 genome editing
421 as described (Chen et al, 2016; Yang et al, 2014). Two guide RNAs targeting the 5th (5'-
422 CATATGGTAACATTGACCCAGGG-3') and 7th (5'- CGTCTCTACCAGCTATACAGCGG-3') were
423 *in vitro* transcribed and purified. The sgRNAs/Cas9 RNPs were complexed and electroporated into
424 zygotes from C57BL/6J. The embryos were transplanted to oviducts of pseudopregnant CD-1
425 foster females and founders' toe were biopsied to extract gDNA. Truncation of the target region
426 was confirmed by gDNA PCR with F3 (5'-CACTTTTCCTGCCTCTGTGTCC-3') and R3 (5'-
427 AGCATCTCCCACTTCCTGTGAC-3') primers. The amplicons were Sanger sequenced and
428 founder females with 4126bp or 4128bp truncation at the genomic region (*4126del* and *4135del*)
429 were mated with C57BL/6 WT mice to confirm the germline transmission of the alleles. Two mutant
430 mice lines were maintained and genotyped with F3-R3 pairs for the mutant allele and F2 (5'-
431 TTGTGGTGGTGGGGAGATAG-3')-R2 (5'-GTGGTGATGGACGGGTGT-3') pair for WT allele.
432
433 **Mouse sperm preparation**
434 Sperm were collected from cauda epididymis of the adult mice by swim-out in M2 medium (EMD
435 Millipore). To induce capacitation, the epididymal sperm were incubated in human tubular fluid
436 (HTF; EMD Millipore) at 2.0 x 10^6 cells/ml concentration for 90 minutes at 37 °C, 5% CO_2 condition.
437
438 **Mammalian Cell culture and transient protein expression**
439 Human embryonic kidney 293T cells (ATTC) were cultured in DMEM (Gibco) supplemented with
440 10% FBS (Gibco) and 1X Pen/Strep (Gibco) at 37 °C, 5% CO_2 condition. Cultured cells were
441 transfected with Lipofectamine 2000 (Invitrogen) or polyethylenimine (PEI) to express recombinant
442 protein transiently. Transfected cells were used for co-immunoprecipitation or modified trap-assay.

443
444 **RNA extraction, cDNA synthesis, and PCR**
445 Total RNA was extracted from transfected 293T cells and frozen mouse testes using RNeasy Mini
446 kit (QIAGEN). Extracted RNA was used for cDNA synthesis using iScript cDNA Synthesis kit (BIO-
447 RAD) in accordance with manufacturer's instruction. Synthesized testis cDNAs were used for
448 endpoint PCR or quantitative PCR using OneTaq 2X Master Mix (NEB) or with iTaq Universal
449 SYBR Green Supermix (BIO-RAD), respectively. Primer pairs, F1 (5'-
450 GGCATCTCTCATCCTCGTCT-3') - R1 (5'-AGCCACTCAGGGTGTCAATC-3'), F4 (5'-
451 TTGGCGTCTCAGCACAAAG-3') - R4 (5'-CTCGAAGCTCCAGGGTGT-3'), and F5 (5'-
452 CTGGACCCCGAGAGACTG-3') - R5 (5'-AGTTTTACCCCCGACCTGTG-3') were used for
453 endpoint PCR; E3 (5'-AGCTGGAGGCTAAGGACAGG-3') - E4 (5'-
454 GAGCGGCGATATGTCTGTAA-3') and E7 (5'-GTCAGAGGCTGAAGGAGGAA-3') - E8 (5'-
455 TATCAGTTCTTGGGGCCAGT-3') were used for quantitative PCR. TBP was used to calculate
456 relative transcript levels in mouse testes by ΔΔCt method.
457
458 **Antibodies and reagent**
459 Rabbit polyclonal RSPH3B were described in previous studies (Hwang et al, 2021b). Rabbit
460 polyclonal anti-LRRC23 (α-118, PA5-63449; α-208, PA5-58095), DNAH1 (PA5-57826), DNAH2
461 (PA5-64309), and DNAH9 (PA5-45744) were from Invitrogen. Rabbit polyclonal SEPTIN4 (NBP1-
462 90093) and mouse monoclonal PMCA4 (clone JA9, NB300-569) antibodies was from Novus
463 Biologicals. Mouse monoclonal anti-His-tag (66005-1-Ig) and rabbit polyclonal anti-AKAP3 (13907-
464 1-AP), RSPH9 (23253-1-AP), and RSPH22 (16811-1-AP) were purchased from Proteintech. Rabbit
465 polyclonal TOM20 (sc-11415) was from SantaCruz. Mouse monoclonal anti-acetylated tubulin
466 (AcTub, clone 6-11B-1, 7451), CALM1 (05-173), pTyr (clone 4G10, 05-321), and HA (clone HA-7,
467 H3663) and rabbit polyclonal anti-SEPTIN12 (HPA041128) were from Sigma-Aldrich. Rabbit and
468 mouse monoclonal anti-DYKDDDDK (clone D6W5B, 86861; clone 9A3, 8146) were from Cell
469 Signaling Technology. Rabbit polyclonal ODF2 and AKAP4 were gifted from Dr. Edward M. Eddy.
470 Rabbit anti-RSPH6A sera was gifted from Dr. Masahito Ikawa. HRP-conjugated goat anti-mouse
471 and anti-rabbit IgG were from Jackson ImmunoResearch. Goat anti-rabbit IgG conjugated with
472 Alexa 568, Lectin PNA conjugated with Alexa 647, and Hoechst dye were from Invitrogen.
473
474 **Protein extraction, solubilization, and immunoblotting**
475 ***Testis*** Adult mouse testes were homogenized in 0.32M using dounce homogenizer followed by
476 centrifugation for 15 minutes at 4 °C, 1000 x g to pellet nucleus and debris. Supernatants was
477 collected and centrifuged at 4 °C, 100,000 rpm for an hour to separate cytosolic and microsome
478 fractions. Volume-equivalented cytosolic and microsome fractions were lysed with 2X LDS
479 sampling buffer and denatured by boiling at 75 °C with 50 mM dithiothreitol (DTT) for 2 or 10
480 minutes, respectively, for SDS-PAGE and immunoblotting. Primary antibodies used for
481 immunoblotting were: rabbit polyclonal anti-LRRC23 (α-118 and α-208, both 1:500) and mouse
482 monoclonal anti-AcTub (1:2,000), and calmodulin (1:1,000).
483 ***Epididymal sperm*** Collected epididymal cells were washed with PBS and lysed using 2X LDS
484 by vortexing at room temperature (RT) for 10 minutes to extract whole sperm proteins as described
485 previously (Hwang et al., 2022). The lysates were centrifuged for 10 minutes at 4 °C, 18,000 x g
486 and the supernatant were mixed to 50 mM DTT followed by boiling at 75 °C for 10 minutes for
487 denaturation. The samples were subjected to SDS-PAGE and immunoblotting. The used primary
488 antibodies were: rabbit polyclonal anti-LRRC23 (α-118 and α-208, 1:500), AKAP3 (1:2,000),

489 RSPH9 (1:500), RSPH22 (1:1,000), ODF2 (1:2,000), AKAP4 (1:2,000), and RSPH3 (1:500), rabbit
490 anti-RSPH6A sera (1:500), and mouse monoclonal, PMCA4 (1:2,000), and AcTub (1:20,000).
491 ***293T cells*** 293T cells were lysed using 0.5% Triton X-100 in 10 mM HEPES, 140 mM NaCl,
492 pH7.4 buffer (1X HEPES buffer) for 2 hours at 4 °C with gentle rocking. The lysates were
493 centrifuged at 4 °C, 18,000 x g for 30 minutes. Supernatant with solubilized proteins were used for
494 protein interaction tests or mixed to 1X LDS and 50 mM DTT followed by boiling at 75 °C for 2
495 minutes. Denatured samples were used for immunoblotting. Mouse monoclonal anti-HA (1:4000)
496 and FLAG (1:1000), and rabbit monoclonal anti-FLAG (1:1000) were used for primary antibody.
497 HRP-conjugated goat anti-rabbit and goat anti-mouse IgG were used for secondary antibodies (0.1
498 μg/ml). SuperSignal™ Western Blot Enhancer (Thermo Scientific) was used for testis and sperm
499 immunoblotting with anti-LRRC23 antibody (α-118).
500
501 **Molecular cloning**
502 Human *LRRC23* ORF clone (HG24717-UT, SinoBiological) and the partial region of the human
503 *LRRC23* 5th intron amplified by PCR was subcloned into phCMV3 vector to generate mammalian
504 expression constructs for human *LRRC23* (*phCMV3-FLAG-hLRRC23^{ORF}-HA*, *phCMV3-FLAG-*
505 *hLRRC23^{WT}-HA,* and *phCMV3-FLAG-hLRRC23^{Mut}-HA*). cDNA clones of human *RSPH3* (616166,
506 Horizon Discovery), *RSPH6A* (5270908, Horizon Discovery), *RSPH9* (5296237, Horizon
507 Discovery), and *RSPH22* (OHu31347, GenScript) was subcloned into *phCMV3* to express human
508 RSPH proteins tagged with FLAG at C-termini. A stop codon was placed at the upstream of
509 sequences encoding HA in phCMV3 vector for tagging FLAG at C-termini. ORFs encoding full-
510 length and the predicted mutant LRRC23 were amplified from *phCMV3-FLAG-hLRRC23^{ORF}-HA*
511 constructs and subcloned into *pGEX-6P2* vector to generate *pGEX-6P2-hLRRC23^{WT}* and *pGEX-*
512 *6P2-hLRRC23^{Mut}* constructs tagging with HA at C-termini. ORFs for each construct were amplified
513 using Q5 Hot Start High-Fidelity 2X Master Mix (NEB) and subcloned into linear vectors using
514 NEBuilder HiFi DNA Assembly Kit (NEB)
515
516 **Recombinant protein purification**
517 Bacterial expression constructs were transformed to BL21-CodonPlus(DE3)-RIL competent cells
518 (Agilent Technologies). Fresh colonies were cultured into LB with antibiotics overnight at 37 °C and
519 cultured further after 50 times dilution at 37 °C until OD_{600} values reach to 0.5-0.8. The cultivates
520 were treated with 1mM IPTG to express recombinant proteins and cultured further for 16-18 hours
521 at 16 °C. IPTG-treated bacteria were washed with PBS and eluted with 1X HEPES buffer containing
522 1% Triton X-100 and EDTA-free protease inhibitor cocktail (Roche) The elutes were sonicated and
523 centrifuged at 18,000 x g, 4 °C for 1 hour. Supernatant were collected and incubated with
524 glutathione agarose (Pierce) for overnight at 4 C to purify recombinant GST and GST-tagged
525 human LRRC23^{WT} and LRRC23^{Mut}. The incubated resins were washed with PBS and eluted with
526 1X HEPES buffer supplemented with 10 mM reduced glutathione. The elutes were dialyzed against
527 1X HEPES buffer with 50% glycerol for overnight at 4 °C. Purified proteins were subjected to
528 Coomassie gel staining using Imperial™ Protein Stain (Thermo Scientific) and immunoblotting.
529
530 **Modified trap assay**
531 293T cells to express FLAG-tagged human RSPH proteins transiently were lysed with 1% Triton
532 X-100 in 1X HEPES buffer with EDTA-free protease inhibitor cocktail (Roche) by rocking at 4 °C
533 for 2 hours. The lysates were centrifuged at 18,000 x g for 30 minutes at 4 °C and the supernatant
534 was incubated with Surebeads™ Protein A Magnetic Bead (Bio-rad) conjugated with rabbit
535 monoclonal DYKDDDDK antibody at RT for two hours. The magnetic beads were washed with 1%

536 Triton X-100 in 1X HEPES buffer two times and 0.2% Triton X-100 in 1X HEPES buffer. Purified
537 GST, GST-tagged human LRRC23^{WT} and LRRC23^{Mut} proteins were incubated with the washed
538 magnetic beads in 0.2% Triton X-100 in 1X HEPES buffer at 4 °C for overnight. Incubated magnetic
539 beads were washed with 0.2% Triton X-100 in 1X HEPES buffer for three times and eluted with 2X
540 LDS buffer containing 50 mM DTT followed by denatured 75 °C for 10 minutes.
541
542 **Sperm fluorescence staining**
543 Epididymal sperm cells were washed with PBS and attached on the glass coverslips by
544 centrifugation at 700 x g for 5 minutes. The coverslips were fixed with either 4% PFA in PBS at RT
545 for 10 minutes (SEPTIN4, SEPTIN12, RSPH3, DNAH2, DNAH9, TOM20, and LRRC23) or acetone
546 at – 20 °C for 5 minutes (RSPH9, DNAH1, AKAP4, ODF2, and AcTub). PFA fixed coverslips were
547 washed with PBS three times and permeablized with 0.1% (SEPTIN4 and SEPTIN12), 0.5%
548 (RSPH3, LRRC23, and DNAH9), or 1% (DNAH2) Triton X-100 in PBS at RT for 10 minutes.
549 Acetone-fixed coverslips were rehydrated by washing with 0.1% Triton X-100 in PBS and PBS.
550 Permeablized coverslips were blocked with 10 % normal goat serum in PBS and incubated with
551 primary antibodies in blocking buffer at 4 °C overnight. Used primary antibodies were: Rabbit
552 polyclonal anti-LRRC23 (α-118, 1:100), SEPTIN4 (1 μg/ml), SEPTIN12 (1:100), RSPH3 (10 μg/ml),
553 RSPH9 (1:100), DNAH1 (3 μg/ml), DNAH2 (0.5 μg/ml), DNAH9 (5 μg/ml), TOM20 (1:50), AKAP4
554 (1:100), and ODF2 (1:50), and mouse monoclonal anti-AcTub (1:200). Coverslips were washed
555 with 0.1% Triton X-100 in PBS one time and PBS two times and incubated with either goat anti-
556 rabbit or mouse IgG conjugated with Alexa 568 in blocking buffer at RT for an hour. The coverslips
557 were washed with PBS three times and mounted on the glass slide using Vectasheild (Vector
558 Laboratory). To observe sperm acrosome, PFA-fixed coverslips were incubated with PNA
559 conjugated with Alexa 647 at RT for an hour. Fluorescence stained coverslips were imaged using
560 Zeiss LSM710 Elyra P1 with Plan-Apochrombat 63X/1.40 objective (Carl Zeiss). Hoechst were
561 used for counter staining.
562
563 **Mating test**
564 Adult heterozygous and homozygous *Lrrc23* mutant male mice were housed with adult female mice
565 with normal fertility and monitored over two months. The pregnancy and litter size were recorded.
566
567 **Sperm motility analysis**
568 ***Computer-assisted sperm analysis*** Computer-assisted sperm analysis (CASA) was
569 performed as previous study (Hwang et al, 2022)**.** Briefly, sperm cells at 3.0 x 10^6 cells/ml
570 concentration were loaded in slide chamber (CellVision) and their motility parameters were
571 measured on 37 °C warm-stage. Motility of over 200 sperm was recorded using CMOS video
572 camera (Basler acA1300-200μm, Basler AG) at 50 frame per seconds (fps) through 10x phase
573 contrast objective (CFI Plan Achro 10X/0.25 Ph1 BM, Nikon) equipped in Nikon E200 microscope.
574 The recorded sperm motility was analyzed using Sperm Class Analyzer software (Microptic).
575 ***Sperm swimming path analysis*** Sperm free swimming analysis was conducted as
576 previous study (Hwang et al, 2019; Hwang et al, 2021a). Briefly, sperm cells were transferred to
577 Delta-T culture dish controller (Bioptech) filled with 37 °C HEPES-buffered HTF medium with 0.3%
578 methylcellulose (Chung et al, 2017). Sperm swimming was imaged using pco.edge sCMOS camera
579 in Axio observer Z1 microscope (Carl Zeiss) for 2 seconds with 100 fps. FIJI software (Schindelin
580 et al, 2012) was used to generate overlaid images to show sperm swimming paths.
581 ***Flagellar waveform analysis*** To analyze sperm flagellar waveform, 2.0 x 10^5 cells of
582 capacitated and non-capacitated sperm cells were placed into 37 °C HEPES-buffered HTF medium

583 (Chung et al, 2017) in fibronectin-coated Delta-T culture dish controller (Bioptech). Flagellar
584 movement of the head-tethered sperm was recorded using pco.edge sCMOS camera equipped in
585 Axio observer Z1 microscope (Carl Zeiss) for 2 seconds with 200 fps. Recorded image stacks were
586 applied to generate overlaid images to show flagellar waveform for two beating cycles with FIJI
587 software (Schindelin et al, 2012).
588

589 **Sequence alignment and phylogenetic analysis**

590 Amino acid sequences of human and mouse normal and mutant LRRC23 were aligned using
591 Clustal Omega (https://www.ebi.ac.uk/Tools/msa/clustalo/). Amino acids sequences of LRRC23
592 and LRRC34 orthologs and *Chlamydomonas reinhardtii* RSP15 were aligned with ClustalW for
593 phylogenetic analysis using MEGA7 (Kumar et al, 2016). Pairwise distances between the
594 sequences were calculated with default option. An unrooted phylogenetic tree was generated by
595 maximum-likelihood analysis with 500 bootstrap replications.
596

597 **Protein structure analysis**

598 Radial spoke 2 and RSP15 structures of the *C. reinhardtii* were from RCSC Protein Data Bank,
599 PDB (https://www.rcsb.org/; 7JU4). Predicted structures of human LRRC23 (Q53EV4) and
600 LRRC34 (Q8IZ02) were from AlphaFold Protein Structure Database (Jumper et al, 2021;
601 https://alphafold.ebi.ac.uk/). Protein structures were rendered and visualized by Mol* 3D Viewer at
602 RCSC PDB.
603

604 **Tissue and testicular expression analysis**

605 Transcript expression data of *LRRC23* and *LRRC34* in human tissues was obtained from GTEx
606 and is based on The Human Protein Atlas version 21.0 and Ensembl version 103.38
607 (https://www.proteinatlas.org/about/download). Medians of the normalized transcript per million
608 (nTPM) are used to calculate relative tissue expression levels. Relative tissue expression levels of
609 *LRRC23* and *LRRC34* are represented as heatmap using GraphPad Prism 8.0 (GraphPad
610 Software Inc., San Diego, CA). UMAP images for the single-cell expression of *LRRC23* and
611 *LRRC34* in human testis are obtained from UCSC Cell browser (Soraggi et al, 2021;
612 https://cells.ucsc.edu/?ds=testis).
613

614 **Transmission electron microscopy**

615 Transmission electron microscopy was performed as previous study (Hwang et al, 2021b). Washed
616 epididymal sperm were pelleted by centrifugation and fixed with 2.5% glutaraldehyde and 2%
617 paraformaldehyde in 0.1M cacodylate buffer pH7.0 for 30 minutes at RT and for 1 hour at 4 °C.
618 The fixed pellets were briefly washed with 0.1M cacodylate buffer pH7.0 and placed in 2% agar.
619 The chilled blocks were trimmed and rinsed with 0.1M cacodylate buffer followed by placed in 0.1%
620 tannic acid in 0.1M cacodylate buffer for 1 hour. The samples were washed and post-fixed in 1%
621 osmium tetroxide and 0.15% potassium ferrocyanide in 0.1M cacodylate buffer for 1 hour. Post-
622 fixed samples were rinsed with the cacodylate buffer and distilled water and subjected to en bloc
623 staining in 2% aqueous uranyl acetate for 1 hour. The samples were dehydrated with ethanol series
624 and infiltrated with epoxy resin Embed 812 (Electron Microscopy Scienes). The resins were placed
625 in silicone molds and backed for 24 hours at 60 °C. The blocks were sectioned in 60 nm depth
626 using Leica UltraCut UC7 and the sections were collected on the formvar/carbon-coated grids.
627 Sections on the grids were stained using 2% uranyl acetate and lead citrate. The stained grids were
628 imaged using MORADA CCD camera (Olympus) equipped in FEI Tecnai Biotwin Transmission
629 Electron Microscope (FEI, Hillsboro, OR) at 80 KV.

630
631 **Cryo-electron tomography**
632 ***Grid preparation*** Grids for sample imaging were prepared as a previously report (Leung et
633 al, 2021). The Quantifoil R2/2 gold grids were glow discharged for 30 seconds at 15mA and 1.5 x
634 10^5 cells of WT or *Lrrc23*$^{\Delta/\Delta}$ sperm were loaded on the grids followed by incubation at RT for 1
635 minutes. The grids were blotted manually from the back site for ~4 seconds using a manual plunger
636 freezer and immediately plunged into liquid ethane and stored in liquid nitrogen.
637 ***Cryo-ET data collection*** Prepared grids with proper ice particles were screened using a
638 Glacios microscope (200 KV, ThermoFisher Scientific) at the Yale Science Hill Electron Microscopy
639 Facility. The screened grids were transferred to the Titan Krios microscope (300 KV, ThermoFisher
640 Scientific) equipped with a Bioquantum Energy Filter and a K3 direct electron detector (Gatan) for
641 data collection at the Yale West Campus Electron Microscopy Facility. Data was collected
642 automatically using SerialEM (Mastronarde, 2005). All images were recorded under super-
643 resolution mode with the physical pixel size 3.4 Å (1.7 Å for super resolution movies). 20 and 60 tilt
644 series of WT and *Lrrc23*$^{\Delta/\Delta}$ mouse sperm were collected with the Volta phase plate at a target
645 defocus around -1 µm. Grouped dose-symmetric scheme spanning from -51° to 51° at 3° increment
646 was applied for tilt series acquisition, with a total dose at 100e-/Å2.
647 ***Tomogram reconstruction*** Process of tomogram reconstruction was streamlined using in-
648 house scripts. The movie frames were aligned first using MotionCorr2 and the micrographs were
649 binned with a factor two (Zheng et al, 2016). Tilt series stack was generated using in-house script.
650 The tilt-series was aligned by AreTomo 1.0.6 (Zheng et al, 2022) to generate XF files which are
651 comparable for IMOD (Kremer et al, 1996). The initial CTF parameters were estimated using
652 Ctffind4 (Rohou & Grigorieff, 2015). The tomograms were then reconstructed with a binning factor
653 six with 20.4 Å pixel size by IMOD with SIRT algorithm for visualization, particle picking and initial
654 sub-tomogram averaging.
655
656 **Sub-Tomogram Averaging of 96-nm axonemal doublet repeat**
657 ***Initial alignment using PEET*** MTDs were manually traced in IMOD (Kremer et al, 1996). After
658 manual tracing, a polynomial function with degree five was fitted to each microtubule doublet with
659 24 nm of a sampling distance (Fig EV6C). The polarity of each tomogram is manually determined
660 to reduce the error during subsequent alignment. The 24-nm repeat particles were first aligned
661 using PEET Version 1.15.0 under "Particle model points" and "align particle Y axes" options
662 (Heumann et al, 2011; Nicastro et al, 2006). A published map of 96-nm MTD repeat in WT mouse
663 sperm (EMD-12133; Leung et al, 2021) was low-pass filtered to 60 Å and used as the initial
664 reference. A mask covering two adjacent MTDs was generated with 160 x 160 x 160 nm^3 dimension
665 of sub-tomogram particle. Only "Phi" angle and translational shifts were searched during the
666 alignment. After the initial alignment, positions of the particles were placed at center based on the
667 translational shifts. The Euler angles were extracted and transformed to RELION Euler angle
668 convention (ZYZ) using the MOTL2Relion command in PEET. In-house script was used to gather
669 the coordinates and corresponding Euler angle information for subsequent RELION4 sub-
670 tomogram averaging analysis.
671 ***Refinement and classification*** After the metadata preparation, the sub-tomogram particles were
672 made in RELION4 (Zivanov et al, 2022) with the binning factor of six. Local 3D refinement with a
673 mask covering one 96-nm MTD was performed. After refinement, the features pf 24-nm repeat of
674 outer dynein arm was observed (Fig EV6D). A smaller mask only covering the inner dynein arm
675 and radial spoke was created for the focused classification without alignment (Fig EV6E). After
676 classification, equivalent 96-nm MTD repeat classes were separated (Fig EV6E). One of the

classes was selected for the future process. New sub-tomogram particles with binning factor three and corresponding 10.2 Å of pixel size were generated. Another local refinement was performed with a 96-nm MTD mask. Resolution was estimated using the Fourier shell correlation (FSC) at a cut-off of 0.143 in RELION4 (Zivanov et al, 2022). Details of acquisition parameters and particle numbers are summarized in Table EV3.

Visualization Images for cryo-ET and sub-tomogram averaging were rendered using IMOD (Kremer et al, 1996) and UCSF Chimerax (Goddard et al, 2018).

Statistical analysis

Statistical analyses were performed using Student's t-test or Mann-Whitney U test. Significant differences were considered at *$p \leq 0.05$, **$p<0.01$, and ***$p<0.001$.

Data availability

The structures for radial spokes from WT (EMD-29013) and *LRRC23*$^{\Delta/\Delta}$ (EMD-28606) sperm resolved by cryo-ET and STA are deposited to Electron Microscopy Data Bank (https://ebi.ac.uk/pdbe/emdb).

Acknowledgments

The authors highly appreciate participation of the family members in the study presented here. We also thank Muhammad Umair, Khadim Shah, Imran Ullah, Hammal Khan for their help to visit the family for interviews and participation in clinical assessment, Habibur Rehmen and Rina Raza from Aga Khan Medical Centre for clinical semen analyses, Jong-Nam Oh for preparing samples for WES, Case Porter and Miriam Hill for their help in PCR and Sanger sequencing, the Yale Center for Cellular and Molecular Imaging for assistance in transmission electron microscopy, Dr. Masahito Ikawa from Osaka University for sharing anti-RSPH6A sera. This study was supported by start-up funds from Yale University School of Medicine and National Institute of Child Health and Human Development (R01HD096745) to J-JC; start-up funds from Yale University, National Institute of General Medical Sciences (R35GM142959) to KZ; Pakistan Academy of Sciences (PAS-171) to WA; National Human Genome Research Institute (UM1HG006504) to the Yale Center for Mendelian Genomics. JH was in part supported by Postdoctoral Fellowship from MCI. SN was supported by Pakistan Higher Education Commission International Research Support Initiative Program. JC was in part supported by a Korea University Medical Center Grant. The Genome Sequencing Program Coordinating Center (U24 HG008956) contributed to cross-program scientific initiatives and provided logistical and general study coordination.

Author Contributions

Jae Yeon Hwang: Conceptualization; methodology; formal analysis; data curation; writing - original draft; writing – review and editing. **Pengxin Chai:** Methodology; formal analysis; data curation; writing – original draft. **Shoaib Nawaz:** Investigation; methodology; formal analysis. **Jungmin Choi:** Methodology; formal analysis; data curation. **Francesc Lopez-Giraldez:** Methodology; formal analysis; data curation. **Shabir Hussain:** Investigation. **Kaya Bilguvar;** Formal analysis. **Shrikant Mane:** Formal analysis. **Richard P. Lifton;** Resource. **Wasim Ahmad:** Resource. **Kai Zhang:** Conceptualization; formal analysis; writing – review and editing; resource; funding

acquisition. **Jean-Ju Chung:** Conceptualization; formal analysis; data curation; writing - original draft; writing – review and editing; resource; supervision; funding acquisition.

Disclosure and competing interests statement

The authors declare that they have no conflict of interest.

727 ## References

728 Abbasi F, Miyata H, Shimada K, Morohoshi A, Nozawa K, Matsumura T, Xu Z, Pratiwi P, Ikawa M
729 (2018) RSPH6A is required for sperm flagellum formation and male fertility in mice. *J Cell Sci* **131**

730
731 Auguste Y, Delague V, Desvignes JP, Longepied G, Gnisci A, Besnier P, Levy N, Beroud C,
732 Megarbane A, Metzler-Guillemain C, Mitchell MJ (2018) Loss of Calmodulin- and Radial-Spoke-
733 Associated Complex Protein CFAP251 Leads to Immotile Spermatozoa Lacking Mitochondria and
734 Infertility in Men. *Am J Hum Genet* **103:** 413-420

735
736 Bazan R, Schrofel A, Joachimiak E, Poprzeczko M, Pigino G, Wloga D (2021) Ccdc113/Ccdc96
737 complex, a novel regulator of ciliary beating that connects radial spoke 3 to dynein g and the
738 nexin link. *PLoS Genet* **17:** e1009388

739
740 Browning BL, Browning SR (2011) A fast, powerful method for detecting identity by descent. *The*
741 *American Journal of Human Genetics* **88:** 173-182

742
743 Castleman VH, Romio L, Chodhari R, Hirst RA, de Castro SC, Parker KA, Ybot-Gonzalez P, Emes
744 RD, Wilson SW, Wallis C, Johnson CA, Herrera RJ, Rutman A, Dixon M, Shoemark A, Bush A, Hogg
745 C, Gardiner RM, Reish O, Greene ND, O'Callaghan C, Purton S, Chung EM, Mitchison HM (2009)
746 Mutations in radial spoke head protein genes RSPH9 and RSPH4A cause primary ciliary
747 dyskinesia with central-microtubular-pair abnormalities. *Am J Hum Genet* **84:** 197-209

748
749 Cavarocchi E, Whitfield M, Saez F, Toure A (2022) Sperm Ion Transporters and Channels in
750 Human Asthenozoospermia: Genetic Etiology, Lessons from Animal Models, and Clinical
751 Perspectives. *Int J Mol Sci* **23**

752
753 Chen S, Lee B, Lee AY-F, Modzelewski AJ, He L (2016) Highly efficient mouse genome editing by
754 CRISPR ribonucleoprotein electroporation of zygotes. *Journal of Biological Chemistry* **291:**
755 14457-14467

756
757 Chen Z, Greenan GA, Shiozaki M, Liu Y, Skinner WM, Zhao X, Zhao S, Yan R, Yu Z, Lishko PV,
758 Agard DA, Vale RD (2023) In situ cryo-electron tomography reveals the asymmetric architecture
759 of mammalian sperm axonemes. *Nat Struct Mol Biol* **30:** 360-369

760
761 Chung JJ, Miki K, Kim D, Shim SH, Shi HF, Hwang JY, Cai X, Iseri Y, Zhuang X, Clapham DE (2017)
762 CatSperzeta regulates the structural continuity of sperm Ca(2+) signaling domains and is
763 required for normal fertility. *Elife* **6**

764

765 Curi SM, Ariagno JI, Chenlo PH, Mendeluk GR, Pugliese MN, Sardi Segovia LM, Repetto HE,
766 Blanco AM (2003) Asthenozoospermia: analysis of a large population. *Arch Androl* **49:** 343-349

767

768 Dong C, Wei P, Jian X, Gibbs R, Boerwinkle E, Wang K, Liu X (2015) Comparison and integration
769 of deleteriousness prediction methods for nonsynonymous SNVs in whole exome sequencing
770 studies. *Human molecular genetics* **24:** 2125-2137

771

772 Goddard TD, Huang CC, Meng EC, Pettersen EF, Couch GS, Morris JH, Ferrin TE (2018) UCSF
773 ChimeraX: Meeting modern challenges in visualization and analysis. *Protein Sci* **27:** 14-25

774

775 Gui M, Ma M, Sze-Tu E, Wang X, Koh F, Zhong ED, Berger B, Davis JH, Dutcher SK, Zhang R,
776 Brown A (2021) Structures of radial spokes and associated complexes important for ciliary
777 motility. *Nat Struct Mol Biol* **28:** 29-37

778

779 Han X, Xie H, Wang Y, Zhao C (2018) Radial spoke proteins regulate otolith formation during
780 early zebrafish development. *FASEB J* **32:** 3984-3992

781

782 Heumann JM, Hoenger A, Mastronarde DN (2011) Clustering and variance maps for cryo-
783 electron tomography using wedge-masked differences. *J Struct Biol* **175:** 288-299

784

785 Hwang JY, Mannowetz N, Zhang Y, Everley RA, Gygi SP, Bewersdorf J, Lishko PV, Chung JJ (2019)
786 Dual Sensing of Physiologic pH and Calcium by EFCAB9 Regulates Sperm Motility. *Cell* **177:** 1480-
787 1494 e1419

788

789 Hwang JY, Maziarz J, Wagner GP, Chung JJ (2021a) Molecular Evolution of CatSper in Mammals
790 and Function of Sperm Hyperactivation in Gray Short-Tailed Opossum. *Cells* **10**

791

792 Hwang JY, Nawaz S, Choi J, Wang H, Hussain S, Nawaz M, Lopez-Giraldez F, Jeong K, Dong W, Oh
793 JN, Bilguvar K, Mane S, Lee CK, Bystroff C, Lifton RP, Ahmad W, Chung JJ (2021b) Genetic Defects
794 in DNAH2 Underlie Male Infertility With Multiple Morphological Abnormalities of the Sperm
795 Flagella in Humans and Mice. *Front Cell Dev Biol* **9:** 662903

796

797 Hwang JY, Wang H, Lu Y, Ikawa M, Chung JJ (2022) C2cd6-encoded CatSpertau targets sperm
798 calcium channel to Ca(2+) signaling domains in the flagellar membrane. *Cell Rep* **38:** 110226

799

800 Imhof S, Zhang J, Wang H, Bui KH, Nguyen H, Atanasov I, Hui WH, Yang SK, Zhou ZH, Hill KL
801 (2019) Cryo electron tomography with volta phase plate reveals novel structural foundations of
802 the 96-nm axonemal repeat in the pathogen Trypanosoma brucei. *Elife* **8**

803
804 Inaba K (2011) Sperm flagella: comparative and phylogenetic perspectives of protein
805 components. *Mol Hum Reprod* **17:** 524-538

806
807 Ishikawa T (2017) Axoneme Structure from Motile Cilia. *Cold Spring Harb Perspect Biol* **9**

808
809 Jeanson L, Copin B, Papon JF, Dastot-Le Moal F, Duquesnoy P, Montantin G, Cadranel J, Corvol H,
810 Coste A, Desir J, Souayah A, Kott E, Collot N, Tissier S, Louis B, Tamalet A, de Blic J, Clement A,
811 Escudier E, Amselem S, Legendre M (2015) RSPH3 Mutations Cause Primary Ciliary Dyskinesia
812 with Central-Complex Defects and a Near Absence of Radial Spokes. *Am J Hum Genet* **97:** 153-
813 162

814
815 Jumper J, Evans R, Pritzel A, Green T, Figurnov M, Ronneberger O, Tunyasuvunakool K, Bates R,
816 Zidek A, Potapenko A, Bridgland A, Meyer C, Kohl SAA, Ballard AJ, Cowie A, Romera-Paredes B,
817 Nikolov S, Jain R, Adler J, Back T, Petersen S, Reiman D, Clancy E, Zielinski M, Steinegger M,
818 Pacholska M, Berghammer T, Bodenstein S, Silver D, Vinyals O, Senior AW, Kavukcuoglu K, Kohli
819 P, Hassabis D (2021) Highly accurate protein structure prediction with AlphaFold. *Nature* **596:**
820 583-589

821
822 Kherraf ZE, Amiri-Yekta A, Dacheux D, Karaouzene T, Coutton C, Christou-Kent M, Martinez G,
823 Landrein N, Le Tanno P, Fourati Ben Mustapha S, Halouani L, Marrakchi O, Makni M, Latrous H,
824 Kharouf M, Pernet-Gallay K, Gourabi H, Robinson DR, Crouzy S, Blum M, Thierry-Mieg N, Toure
825 A, Zouari R, Arnoult C, Bonhivers M, Ray PF (2018) A Homozygous Ancestral SVA-Insertion-
826 Mediated Deletion in WDR66 Induces Multiple Morphological Abnormalities of the Sperm
827 Flagellum and Male Infertility. *Am J Hum Genet* **103:** 400-412

828
829 Knowles MR, Ostrowski LE, Leigh MW, Sears PR, Davis SD, Wolf WE, Hazucha MJ, Carson JL,
830 Olivier KN, Sagel SD, Rosenfeld M, Ferkol TW, Dell SD, Milla CE, Randell SH, Yin W, Sannuti A,
831 Metjian HM, Noone PG, Noone PJ, Olson CA, Patrone MV, Dang H, Lee HS, Hurd TW, Gee HY,
832 Otto EA, Halbritter J, Kohl S, Kircher M, Krischer J, Bamshad MJ, Nickerson DA, Hildebrandt F,
833 Shendure J, Zariwala MA (2014) Mutations in RSPH1 cause primary ciliary dyskinesia with a
834 unique clinical and ciliary phenotype. *Am J Respir Crit Care Med* **189:** 707-717

835
836 Kott E, Legendre M, Copin B, Papon JF, Dastot-Le Moal F, Montantin G, Duquesnoy P, Piterboth
837 W, Amram D, Bassinet L, Beucher J, Beydon N, Deneuville E, Houdouin V, Journel H, Just J,
838 Nathan N, Tamalet A, Collot N, Jeanson L, Le Gouez M, Vallette B, Vojtek AM, Epaud R, Coste A,
839 Clement A, Housset B, Louis B, Escudier E, Amselem S (2013) Loss-of-function mutations in
840 RSPH1 cause primary ciliary dyskinesia with central-complex and radial-spoke defects. *Am J Hum*
841 *Genet* **93:** 561-570

842

843 Krause I, Pohler U, Grosse S, Shebl O, Petek E, Chandra A, Ebner T (2016) Characterization of the
844 injection funnel during intracytoplasmic sperm injection reflects cytoplasmic maturity of the
845 oocyte. *Fertil Steril* **106:** 1101-1106

846

847 Kremer JR, Mastronarde DN, McIntosh JR (1996) Computer visualization of three-dimensional
848 image data using IMOD. *J Struct Biol* **116:** 71-76

849

850 Kubo S, Yang SK, Black CS, Dai D, Valente-Paterno M, Gaertig J, Ichikawa M, Bui KH (2021)
851 Remodeling and activation mechanisms of outer arm dyneins revealed by cryo-EM. *EMBO Rep*
852 **22:** e52911

853

854 Kumar S, Stecher G, Tamura K (2016) MEGA7: Molecular Evolutionary Genetics Analysis Version
855 7.0 for Bigger Datasets. *Mol Biol Evol* **33:** 1870-1874

856

857 Lek M, Karczewski KJ, Minikel EV, Samocha KE, Banks E, Fennell T, O'Donnell-Luria AH, Ware JS,
858 Hill AJ, Cummings BB (2016) Analysis of protein-coding genetic variation in 60,706 humans.
859 *Nature* **536:** 285-291

860

861 Leung MR, Roelofs MC, Ravi RT, Maitan P, Henning H, Zhang M, Bromfield EG, Howes SC,
862 Gadella BM, Bloomfield-Gadelha H, Zeev-Ben-Mordehai T (2021) The multi-scale architecture of
863 mammalian sperm flagella and implications for ciliary motility. *EMBO J* **40:** e107410

864

865 Li H (2013) Aligning sequence reads, clone sequences and assembly contigs with BWA-MEM.
866 *arXiv preprint arXiv:13033997*

867

868 Lin J, Heuser T, Carbajal-Gonzalez BI, Song K, Nicastro D (2012) The structural heterogeneity of
869 radial spokes in cilia and flagella is conserved. *Cytoskeleton (Hoboken)* **69:** 88-100

870

871 Lin J, Yin W, Smith MC, Song K, Leigh MW, Zariwala MA, Knowles MR, Ostrowski LE, Nicastro D
872 (2014) Cryo-electron tomography reveals ciliary defects underlying human RSPH1 primary ciliary
873 dyskinesia. *Nat Commun* **5:** 5727

874

875 Liu S, Zhang J, Kherraf ZE, Sun S, Zhang X, Cazin C, Coutton C, Zouari R, Zhao S, Hu F, Fourati Ben
876 Mustapha S, Arnoult C, Ray PF, Liu M (2021) CFAP61 is required for sperm flagellum formation
877 and male fertility in human and mouse. *Development* **148**

878

879 Ma A, Zeb A, Ali I, Zhao D, Khan A, Zhang B, Zhou J, Khan R, Zhang H, Zhang Y, Khan I, Shah W, Ali
880 H, Javed AR, Ma H, Shi Q (2021) Biallelic Variants in CFAP61 Cause Multiple Morphological
881 Abnormalities of the Flagella and Male Infertility. *Front Cell Dev Biol* **9:** 803818

882
883 Manichaikul A, Mychaleckyj JC, Rich SS, Daly K, Sale M, Chen W-M (2010) Robust relationship
884 inference in genome-wide association studies. *Bioinformatics* **26:** 2867-2873

885
886 Martinez G, Beurois J, Dacheux D, Cazin C, Bidart M, Kherraf ZE, Robinson DR, Satre V, Le Gac G,
887 Ka C, Gourlaouen I, Fichou Y, Petre G, Dulioust E, Zouari R, Thierry-Mieg N, Toure A, Arnoult C,
888 Bonhivers M, Ray P, Coutton C (2020) Biallelic variants in MAATS1 encoding CFAP91, a
889 calmodulin-associated and spoke-associated complex protein, cause severe astheno-
890 teratozoospermia and male infertility. *J Med Genet* **57:** 708-716

891
892 Mastronarde DN (2005) Automated electron microscope tomography using robust prediction of
893 specimen movements. *J Struct Biol* **152:** 36-51

894
895 McKenna A, Hanna M, Banks E, Sivachenko A, Cibulskis K, Kernytsky A, Garimella K, Altshuler D,
896 Gabriel S, Daly M (2010) The Genome Analysis Toolkit: a MapReduce framework for analyzing
897 next-generation DNA sequencing data. *Genome research* **20:** 1297-1303

898
899 Nawaz S, Ullah MI, Hamid BS, Nargis J, Nawaz M, Hussain S, Ahmad W (2021) A loss-of-function
900 variant in DNA mismatch repair gene MLH3 underlies severe oligozoospermia. *J Hum Genet* **66:**
901 725-730

902
903 Nicastro D, Schwartz C, Pierson J, Gaudette R, Porter ME, McIntosh JR (2006) The molecular
904 architecture of axonemes revealed by cryoelectron tomography. *Science* **313:** 944-948

905
906 World Health Organization (2010) *WHO laboratory manual for the examination and processing*
907 *of human semen*, 5th ed edn. Geneva: World Health Organization.

908
909 Padma P, Satouh Y, Wakabayashi K, Hozumi A, Ushimaru Y, Kamiya R, Inaba K (2003)
910 Identification of a novel leucine-rich repeat protein as a component of flagellar radial spoke in
911 the Ascidian Ciona intestinalis. *Mol Biol Cell* **14:** 774-785

912
913 Pigino G, Bui KH, Maheshwari A, Lupetti P, Diener D, Ishikawa T (2011) Cryoelectron tomography
914 of radial spokes in cilia and flagella. *J Cell Biol* **195:** 673-687

915
916 Ralston KS, Lerner AG, Diener DR, Hill KL (2006) Flagellar motility contributes to cytokinesis in
917 Trypanosoma brucei and is modulated by an evolutionarily conserved dynein regulatory system.
918 *Eukaryot Cell* **5:** 696-711

919

920 Rao Q, Han L, Wang Y, Chai P, Kuo YW, Yang R, Hu F, Yang Y, Howard J, Zhang K (2021) Structures
921 of outer-arm dynein array on microtubule doublet reveal a motor coordination mechanism. *Nat*
922 *Struct Mol Biol* **28:** 799-810

923
924 Rohou A, Grigorieff N (2015) CTFFIND4: Fast and accurate defocus estimation from electron
925 micrographs. *J Struct Biol* **192:** 216-221

926
927 Satouh Y, Inaba K (2009) Proteomic characterization of sperm radial spokes identifies a novel
928 spoke protein with an ubiquitin domain. *FEBS Lett* **583:** 2201-2207

929
930 Schindelin J, Arganda-Carreras I, Frise E, Kaynig V, Longair M, Pietzsch T, Preibisch S, Rueden C,
931 Saalfeld S, Schmid B, Tinevez JY, White DJ, Hartenstein V, Eliceiri K, Tomancak P, Cardona A
932 (2012) Fiji: an open-source platform for biological-image analysis. *Nat Methods* **9:** 676-682

933
934 Shamseldin HE, Shaheen R, Ewida N, Bubshait DK, Alkuraya H, Almardawi E, Howaidi A, Sabr Y,
935 Abdalla EM, Alfaifi AY, Alghamdi JM, Alsagheir A, Alfares A, Morsy H, Hussein MH, Al-Muhaizea
936 MA, Shagrani M, Al Sabban E, Salih MA, Meriki N, Khan R, Almugbel M, Qari A, Tulba M,
937 Mahnashi M, Alhazmi K, Alsalamah AK, Nowilaty SR, Alhashem A, Hashem M, Abdulwahab F,
938 Ibrahim N, Alshidi T, AlObeid E, Alenazi MM, Alzaidan H, Rahbeeni Z, Al-Owain M, Sogaty S,
939 Seidahmed MZ, Alkuraya FS (2020) The morbid genome of ciliopathies: an update. *Genet Med*
940 **22:** 1051-1060

941
942 Shen Q, Martinez G, Liu H, Beurois J, Wu H, Amiri-Yekta A, Liang D, Kherraf ZE, Bidart M, Cazin C,
943 Celse T, Satre V, Thierry-Mieg N, Whitfield M, Toure A, Song B, Lv M, Li K, Liu C, Tao F, He X,
944 Zhang F, Arnoult C, Ray PF, Cao Y, Coutton C (2021) Bi-allelic truncating variants in CFAP206
945 cause male infertility in human and mouse. *Hum Genet* **140:** 1367-1377

946
947 Sironen A, Shoemark A, Patel M, Loebinger MR, Mitchison HM (2020) Sperm defects in primary
948 ciliary dyskinesia and related causes of male infertility. *Cell Mol Life Sci* **77:** 2029-2048

949
950 Slabbert M, du Plessis SS, Huyser C (2015) Large volume cryoprotectant-free vitrification: an
951 alternative to conventional cryopreservation for human spermatozoa. *Andrologia* **47:** 594-599

952
953 Smith EF, Sale WS (1992) Regulation of dynein-driven microtubule sliding by the radial spokes in
954 flagella. *Science* **257:** 1557-1559

955
956 Smith EF, Yang P (2004) The radial spokes and central apparatus: mechano-chemical transducers
957 that regulate flagellar motility. *Cell Motil Cytoskeleton* **57:** 8-17

958

959 Soraggi S, Riera M, Meyts R-D, Schierup MH, Almstrup K (2021) Evaluating genetic causes of
960 azoospermia: What can we learn from a complex cellular structure and single-cell
961 transcriptomics of the human testis? *Human Genetics* **140:** 183-201

962
963 Toure A, Martinez G, Kherraf ZE, Cazin C, Beurois J, Arnoult C, Ray PF, Coutton C (2021) The
964 genetic architecture of morphological abnormalities of the sperm tail. *Hum Genet* **140:** 21-42

965
966 Urbanska P, Song K, Joachimiak E, Krzemien-Ojak L, Koprowski P, Hennessey T, Jerka-Dziadosz
967 M, Fabczak H, Gaertig J, Nicastro D, Wloga D (2015) The CSC proteins FAP61 and FAP251 build
968 the basal substructures of radial spoke 3 in cilia. *Mol Biol Cell* **26:** 1463-1475

969
970 Van der Auwera GA, Carneiro MO, Hartl C, Poplin R, Del Angel G, Levy‐Moonshine A, Jordan T,
971 Shakir K, Roazen D, Thibault J (2013) From FastQ data to high‐confidence variant calls: the
972 genome analysis toolkit best practices pipeline. *Current protocols in bioinformatics* **43:** 11.10.
973 11-11.10. 33

974
975 Viswanadha R, Sale WS, Porter ME (2017) Ciliary Motility: Regulation of Axonemal Dynein
976 Motors. *Cold Spring Harb Perspect Biol* **9**

977
978 Witman GB, Plummer J, Sander G (1978) Chlamydomonas flagellar mutants lacking radial spokes
979 and central tubules. Structure, composition, and function of specific axonemal components. *J*
980 *Cell Biol* **76:** 729-747

981
982 Yang H, Wang H, Jaenisch R (2014) Generating genetically modified mice using CRISPR/Cas-
983 mediated genome engineering. *Nature protocols* **9:** 1956-1968

984
985 Yang P, Diener DR, Yang C, Kohno T, Pazour GJ, Dienes JM, Agrin NS, King SM, Sale WS, Kamiya R,
986 Rosenbaum JL, Witman GB (2006) Radial spoke proteins of Chlamydomonas flagella. *J Cell Sci*
987 **119:** 1165-1174

988
989 Yin W, Livraghi-Butrico A, Sears PR, Rogers TD, Burns KA, Grubb BR, Ostrowski LE (2019) Mice
990 with a Deletion of Rsph1 Exhibit a Low Level of Mucociliary Clearance and Develop a Primary
991 Ciliary Dyskinesia Phenotype. *Am J Respir Cell Mol Biol* **61:** 312-321

992
993 Yoke H, Ueno H, Narita A, Sakai T, Horiuchi K, Shingyoji C, Hamada H, Shinohara K (2020) Rsph4a
994 is essential for the triplet radial spoke head assembly of the mouse motile cilia. *PLoS Genet* **16:**
995 e1008664

996

997 Zhang X, Sun J, Lu Y, Zhang J, Shimada K, Noda T, Zhao S, Koyano T, Matsuyama M, Zhou S, Wu J,
998 Ikawa M, Liu M (2021) LRRC23 is a conserved component of the radial spoke that is necessary
999 for sperm motility and male fertility in mice. *J Cell Sci* **134**

1000
1001 Zhao Y, Pinskey J, Lin J, Yin W, Sears PR, Daniels LA, Zariwala MA, Knowles MR, Ostrowski LE,
1002 Nicastro D (2021) Structural insights into the cause of human RSPH4A primary ciliary dyskinesia.
1003 *Mol Biol Cell* **32:** 1202-1209

1004
1005 Zheng S, Wolff G, Greenan G, Chen Z, Faas FGA, Barcena M, Koster AJ, Cheng Y, Agard DA (2022)
1006 AreTomo: An integrated software package for automated marker-free, motion-corrected cryo-
1007 electron tomographic alignment and reconstruction. *J Struct Biol X* **6:** 100068

1008
1009 Zheng SQ, Palovcak E, Armache J-P, Cheng Y, Agard DA (2016) Anisotropic correction of beam-
1010 induced motion for improved single-particle electron cryo-microscopy. *bioRxiv***:** 061960

1011
1012 Zheng W, Li F, Ding Z, Liu H, Zhu L, Xu C, Li J, Gao Q, Wang Y, Fu Z, Peng C, Yan X, Zhu X, Cong Y
1013 (2021) Distinct architecture and composition of mouse axonemal radial spoke head revealed by
1014 cryo-EM. *Proc Natl Acad Sci U S A* **118**

1015
1016 Zhu X, Liu Y, Yang P (2017) Radial Spokes-A Snapshot of the Motility Regulation, Assembly, and
1017 Evolution of Cilia and Flagella. *Cold Spring Harb Perspect Biol* **9**

1018
1019 Zivanov J, Otón J, Ke Z, von Kügelgen A, Pyle E, Qu K, Morado D, Castaño-Díez D, Zanetti G,
1020 Bharat TAM, Briggs JAG, Scheres SHW (2022) A Bayesian approach to single-particle electron
1021 cryo-tomography in RELION-4.0. *bioRxiv***:** 2022.2002.2028.482229

1022
1023 Zou W, Lv Y, Liu ZI, Xia P, Li H, Jiao J (2020) Loss of Rsph9 causes neonatal hydrocephalus with
1024 abnormal development of motile cilia in mice. *Sci Rep* **10:** 12435

1025

1026

1027 **Figure Legends**

1028

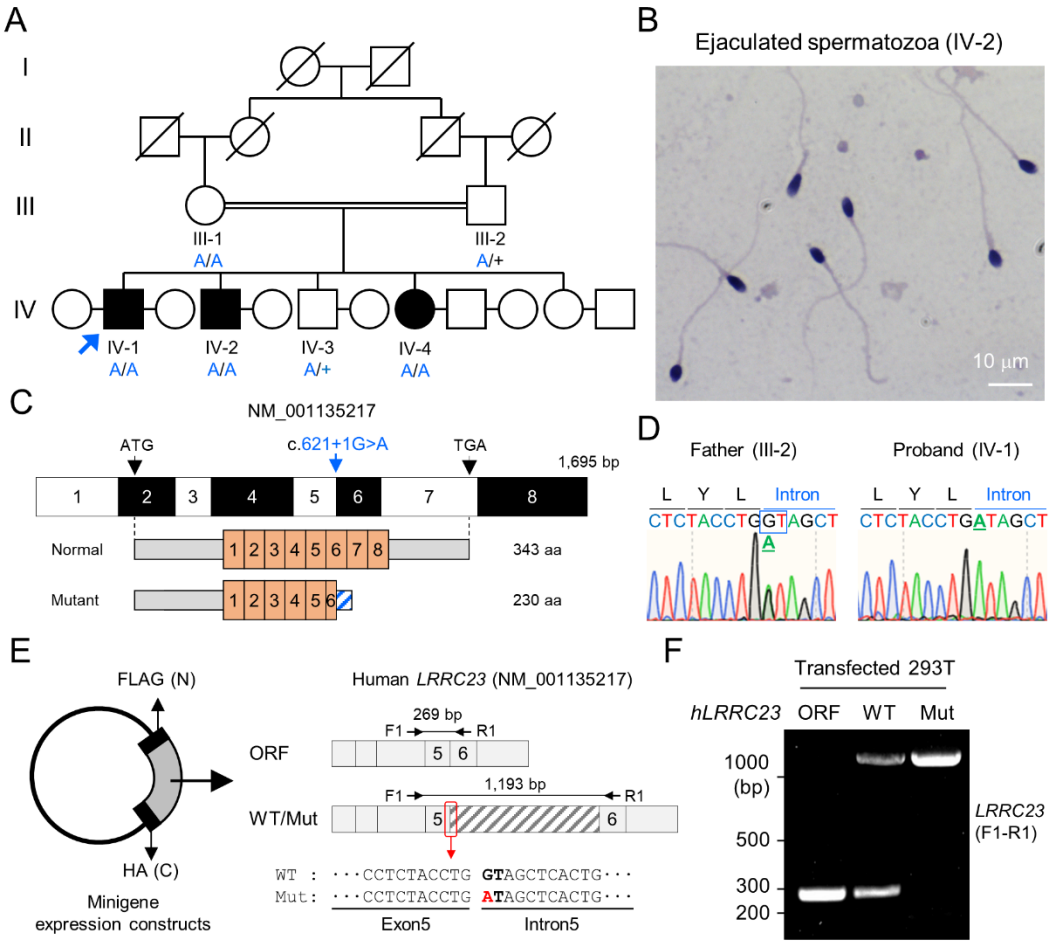

1029

1030

1031 **Figure 1. A bi-allelic splicing donor site variant in *LRRC23* was identified from**
1032 **asthenozoospermia patients.**

1033 A A consanguineous pedigree with two infertile males (IV-1 and IV-2). IV-1 was subjected for
1034 WES (arrow). Genotypes of the variant (blue) in all family members included in this study (III-1, III-
1035 2, IV-1, IV-2, IV-3, and IV-4) are confirmed by Sanger sequencing. +, wild-type allele. An infertile
1036 female sibling (IV-4) is marked in black circle.

1037 B Papanicolaou-stained sperm from the infertile male (IV-2).

1038 C Mapping of the LRRC23 variant. Mutation of G to A at the splicing donor site in the 5th intron
1039 is predicted to prevent *LRRC23* mRNA from splicing.

1040 D Sequencing chromatograms presenting the *LRRC23* variant in the infertile male (IV-1) and
1041 his father (III-2). The variant is underlined and normal splicing donor site (GT) is boxed.

1042 E, F Minigene assay for testing altered splicing of *LRRC23* by the variant. (E) Minigene
1043 constructs expressing *LRRC23* ORF containing the 5th intron (sashed) with wild-type (WT) or
1044 mutant (Mut, red) splicing donor site were generated. The constructs are tagged with FLAG and

1045 HA at N- and C-termini, respectively. (F) RT-PCR of the 293T cells transfected with the minigene
1046 constructs reveals the 5th intron is not spliced out and retained by the variant. Intron-spanning
1047 primers, F1 and R1, are used. Repeated three times with biological replications.

1048

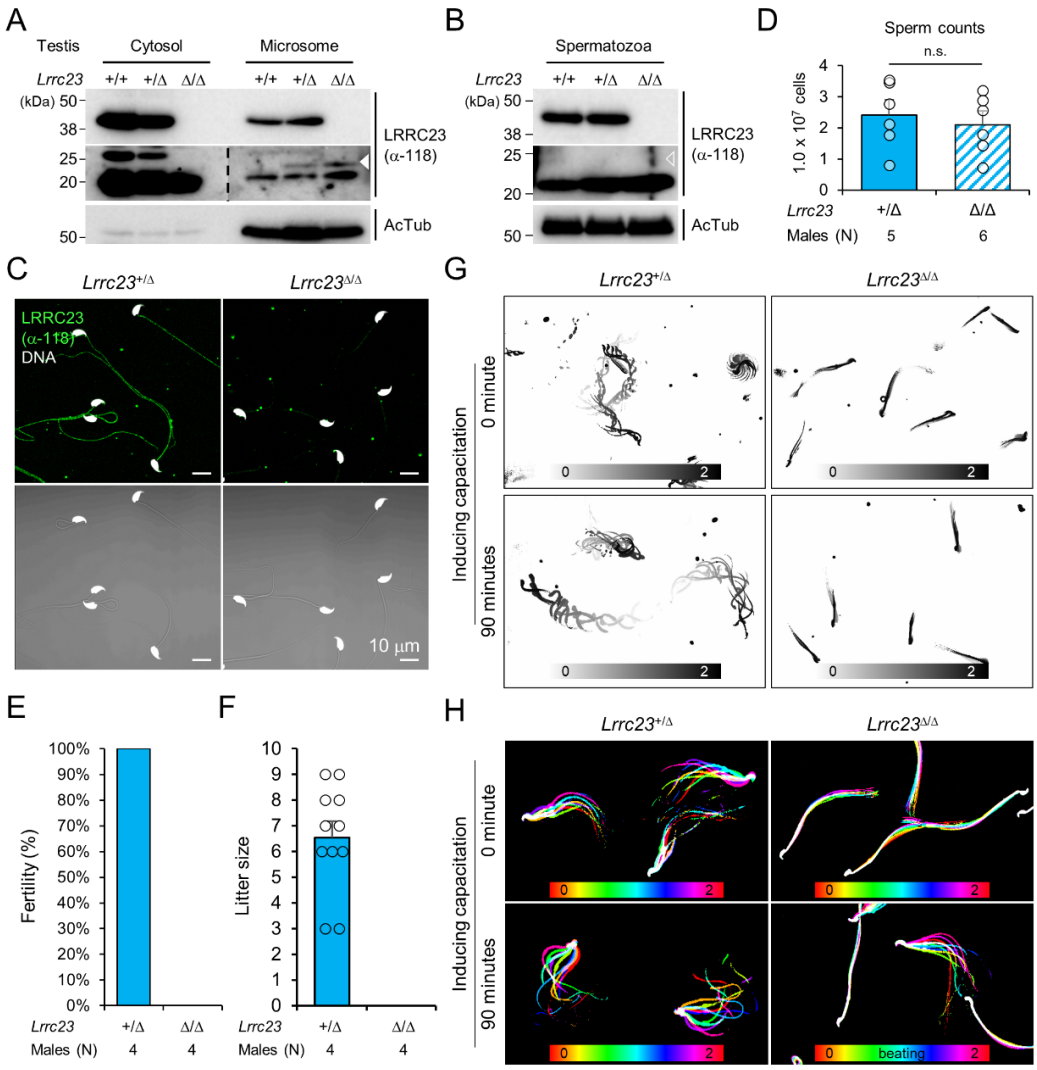

Figure 2. *Lrrc23* mutant mice mimicking human splice variant phenocopy male infertility and reduced sperm motility.

A, B Immunoblotting of LRRC23 in testis (A) and epididymal sperm (B) from mutant male mice. Truncated LRRC23 (arrowheads) is detected from testis microsome fraction (filled), but not in mature sperm (empty), of heterozygous (+/Δ) and homozygous (Δ/Δ) males. Acetylated tubulin (AcTub) is a loading control. Experiments were performed with three biological replications.

C Confocal images of immunostained LRRC23 in *Lrrc23*$^{+/\Delta}$ and *Lrrc23*$^{\Delta/\Delta}$ epididymal sperm Experiments were repeated with three biological replications.

D Epididymal sperm counts. n.s., not significant.

E Pregnancy rate of *Lrrc23*$^{+/\Delta}$ and *Lrrc23*$^{\Delta/\Delta}$ males.

F Number of litters from fertile females mated with *Lrrc23*$^{+/\Delta}$ and *Lrrc23*$^{\Delta/\Delta}$ males.

G Swimming trajectory of *Lrrc23*$^{+/\Delta}$ and *Lrrc23*$^{\Delta/\Delta}$ sperm in viscous media (0.3% methylcellulose). Swimming trajectory for 2 seconds is overlaid. Experiments were performed with

1063 three biological replications. See Movie EV1.

1064 H Flagellar waveforms of *Lrrc23*$^{+/\Delta}$ and *Lrrc23*$^{\Delta/\Delta}$ sperm before (0 minute) and after (90
1065 minutes) inducing capacitation. Flagellar movements for two beat cycles are overlaid and color
1066 coded in time. Experiments were performed with three biological replications. See Movie EV2.

1067 Data information: In (A-C), samples from WT were used for positive or negative control of normal
1068 or truncated LRRC23. In (D, F), circles indicate sperm counts from individual males (D) and pup
1069 numbers from each litter (F), and data represented as mean ± SEM (D, Mann-whiteny U test; F,
1070 Student's t-test). n.s., non-significant.

1071

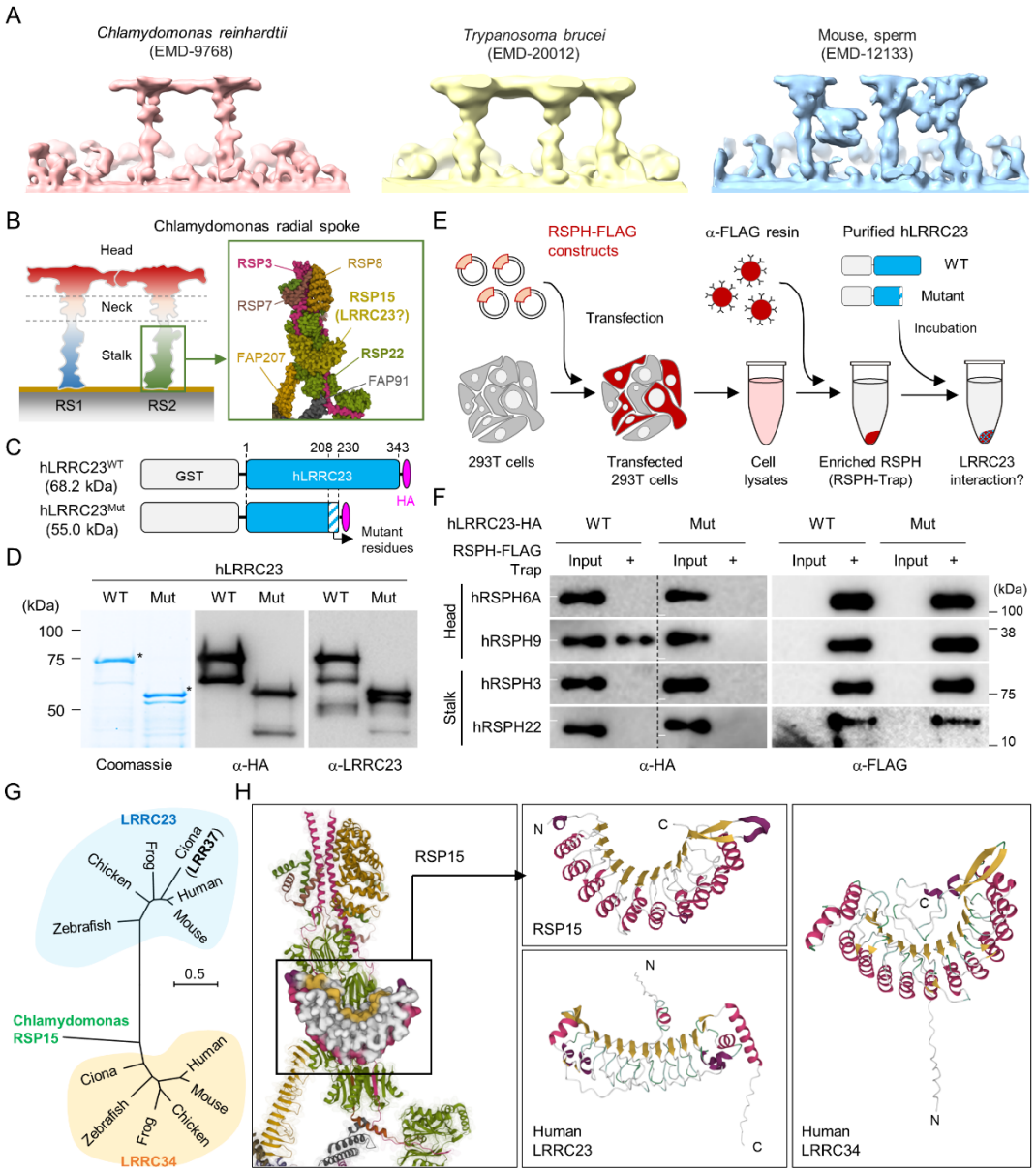

Figure 3. C-terminal truncation of human LRRC23 by the splicing site mutation prevents its interaction with radial spoke (RS) head.

A Sub-tomogram averaging images of RSs from *Chlamydomonas reinhardtii* (*left*), *Trypanosoma brucei* (*middle*), and mouse sperm (*right*). Original data from Electron Microscopy Data Bank was rendered.

B Structure of RS in *C. reinhardtii*. A schematic cartoon shows the RS1 and 2. The structure of RS2 stalk is shown in inset (PDB Id: 7JRJ).

C, D Purification of normal (hLRRC23^{WT}) and the mutant human LRRC23 (hLRRC23^{Mut}) by the splicing site mutation (c.621+1G>A) in this study. (C) Diagrams for the purified recombinant normal and mutant proteins tagged with tagged with GST and HA at N- and C-termini, respectively. (D)

1083 Purified proteins by Coomassie blue staining (*left*) and immunoblotting with α-HA (*middle*) and a-
1084 LRRC23 (*right*). Proteins matched to the predicted size were marked with asterisks.

1085 E A cartoon of the RSPH-trap approach to test LRRC23 interaction with RS proteins.
1086 Individual human RS proteins tagged with FLAG (RSPH-FLAG) are expressed in 293T cells and
1087 enriched by α-FLAG resin from cell lysates. The recombinant RSPH proteins were incubated with
1088 the purified hLRRC23^{WT} or hLRRC23^{Mut} and subjected to immunoblotting.

1089 F Interaction of hLRRC23 to a RS head component, RSPH9. The purified hLRRC23 were
1090 incubated with the RSPH-Trap (RS head, RSPH6A and RSPH9; stalk, RSPH3 and RSPH22) and
1091 subjected to immunoblotting. 5% amount of the hLRRC23s used for the trap assay were loaded as
1092 inputs. White lines in individual α-HA blot images indicate marker information (75 kDa, *left*; 50 kDa,
1093 *right*). Experiments were repeated four times. Purified GST was used for negative control (Fig
1094 EV4B). Experiments were repeated three times with biological replications.

1095

1096 G A phylogenetic tree constructed by Maximum-likelihood analysis of the protein sequences
1097 of the *C. reinhardtii* RSP15 and the orthologs of LRRC23 and LRRC34. LRR37, the first LRRC23
1098 ortholog identified in *Ciona intestinalis* is marked in bold.

1099 H Comparison of the reported RSP15 from *C. reinhardtii* and the predicted structure of
1100 LRRC23 and LRRC34 from human. Atomic structure of the *C. reinhardtii* RS2 containing RSP15
1101 are represented by ribbon (RS2) and surface (RSP15) diagram (*left*, PDB Id: 7JU4). Ribbon
1102 diagrams of *C. reinhardtii* RSP15 and AlphaFold-predicted human LRRC23 (*middle*) and LRRC34
1103 (*right*) are shown for structural comparison. Secondary structures are color-coded. Different from
1104 *C. reinhardtii* RSP15 and LRRC34, LRRC23 does not display repeated α-helix (magenta) between
1105 β-sheets (gold).

1106

1107

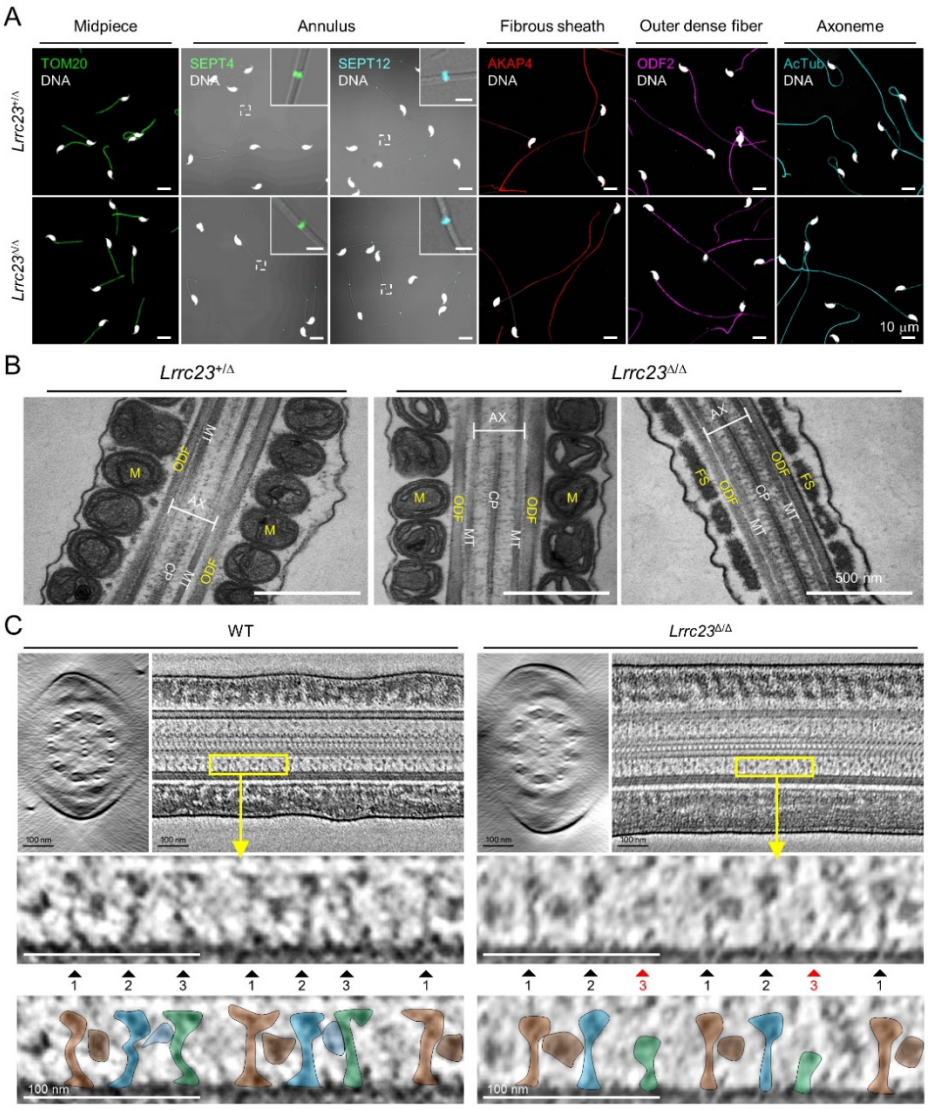

Figure 4. LRRC23 mutation disrupts the third radial spoke (RS) in sperm flagellum.

A Immunostaining of flagellar proteins in different compartments. Shown are midpiece (TOM20), annulus (SEPT4 and SEPT12), fibrous sheath (AKAP4), outer dense fiber (ODF2), and axoneme (acetylated tubulin, AcTub) in *Lrrc23*$^{+/\Delta}$ (*top*) and *Lrrc23*$^{\Delta/\Delta}$ (*bottom*) sperm. Magnified insets are represented for annulus proteins (scale bars in insets = 2μm). Fluorescence and corresponding DIC images are merged. Sperm heads were counter stained with Hoechst. *Lrrc23*$^{+/\Delta}$ sperm were used for positive control. Experiments were performed with three biological replications.

B Transmission electron microscopy images of *Lrrc23*$^{+/\Delta}$ (*left*) and *Lrrc23*$^{\Delta/\Delta}$ (*right*) sperm. Shown are longitudinal section of sperm flagella. M, mitochondria; ODF, outer dense fiber; AX, axoneme; CP, central pair; MT, microtubule; FS, fibrous sheath. *Lrrc23*$^{+/\Delta}$ sperm were used for positive control.

C Cryo-electron tomography (cryo-ET) of WT and *Lrrc23*$^{\Delta/\Delta}$ sperm flagella. Shown are representative tomographic slices from WT (*left*) and *Lrrc23*$^{\Delta/\Delta}$ sperm (*right*). The 9+2 axonemal structure are shown in both WT and *Lrrc23*$^{\Delta/\Delta}$ in cross-sectional view (*left*). Axonemal structures

1123 are shown with proximal side of the flagellum on the left in longitudinal view (*right*; see Movie EV3).
1124 Magnified insets (*bottom*) reveal that RS1, 2, and 3 are shown in WT sperm (*left*, filled arrowheads)
1125 but RS3, especially head part, is not clearly visible (*right*, red arrowheads) in *Lrrc23*$^{\Delta/\Delta}$ sperm. or
1126 WT sperm were used for positive control.

1127

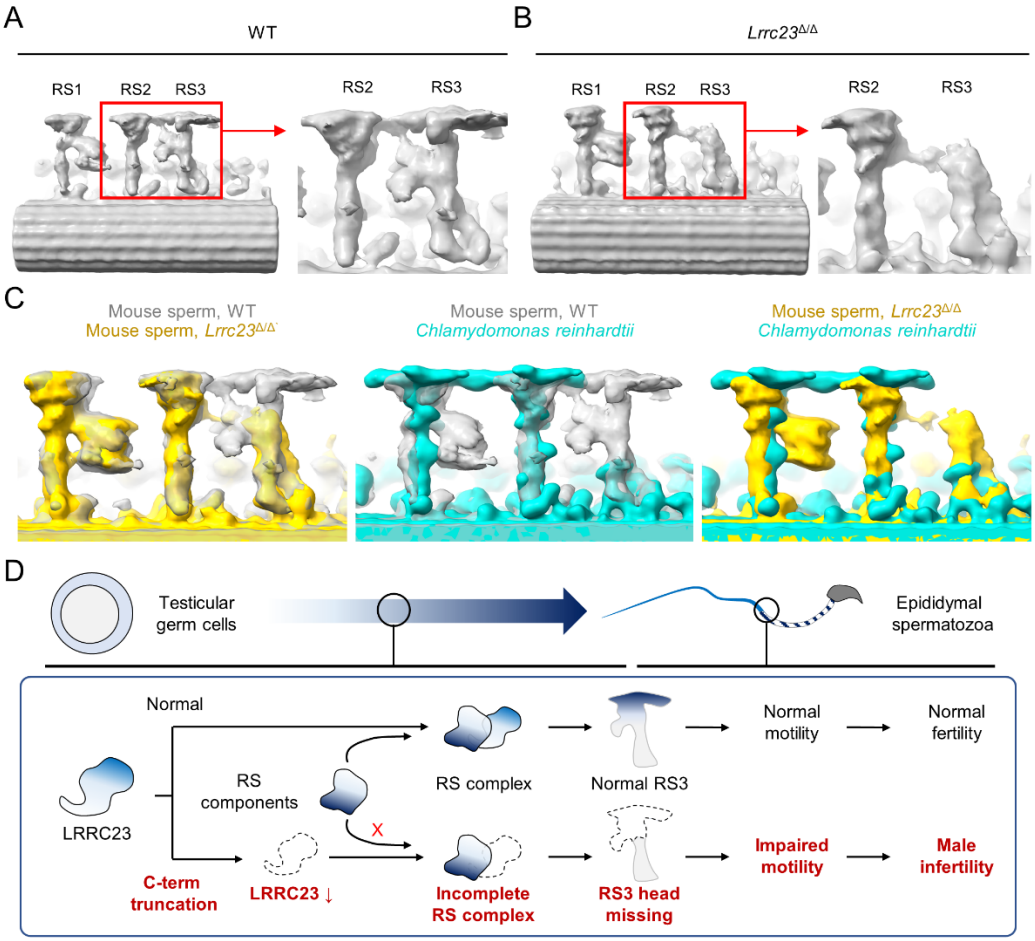

Figure 5. Head of the third radial spoke is absent in *Lrrc23*$^{\Delta/\Delta}$ sperm flagella.

A, B Sub-tomogram averaging (STA) to analyze structural defects at radial spoke (RS) of WT (A) and *Lrrc23*$^{\Delta/\Delta}$ sperm (B). Shown are STA images resulted from 96-nm doublet repeats from WT and *Lrrc23*$^{\Delta/\Delta}$ sperm. RS2 and 3 are magnified and density to represent RS3 head and the bridge between RS2 and RS3 (red circle) is missed in *Lrrc23*$^{\Delta/\Delta}$ sperm specifically.

C Overwrapped STA images from 96 nm-doublet repeats from WT (gray) and *Lrrc23*$^{\Delta/\Delta}$ (gold) sperm, and *Chlamydomonas reinhardtii* (cyan).

D A proposed model of impaired sperm motility and male infertility by the LRRC23 loss of function.